

Magnetic Signature Mapping of a Moving Ship Using a Fleet of Autonomous Underwater Vehicles

A Thesis

Presented in Partial Fulfillment of the Requirements for the

Degree of Master of Science

with a

Major in Mechanical Engineering

in the

College of Graduate Studies

University of Idaho

By

Christopher Walker

July 2012

Major Professor: Michael Anderson, Ph.D.

Authorization to Submit Thesis

This thesis of Christopher Walker, submitted for the degree of Master of Science with a major in Mechanical Engineering and titled “Magnetic Signature Mapping of a Moving Ship Using a Fleet of Autonomous Underwater Vehicles,” has been reviewed in final form. Permission, as indicated by the signatures and dates given below, is now granted to submit final copies to the College of Graduate Studies for approval.

Major Professor _____ Date _____

Michael Anderson, Ph.D.

Committee Members _____ Date _____

Dean Edwards, Ph.D.

_____ Date _____

Eric Wolbrecht, Ph.D.

Department Administrator _____ Date _____

John Crepeau, Ph.D.

Discipline’s College Dean _____ Date _____

Larry Stauffer, Ph.D.

Final Approval and Acceptance by the College of Graduate Studies

_____ Date _____

Jie Chen, Ph.D.

Abstract

A fleet of autonomous underwater vehicles has been developed by the University of Idaho to enable the measurement of the magnetic signature of naval surface vessels during forward area operations. Each autonomous underwater vehicle (AUV) is equipped with a fluxgate magnetometer, a GPS receiver, an inertial measurement unit, and an acoustic modem as well as several other sensors. The position of each AUV relative to the surface vessel and the magnetic field at that position must both be accurately known in order to provide a useful assessment of the surface vessel magnetic signature.

This document describes the first known magnetic signature mapping of a surface vessel by a fleet of AUVs. To create an accurate field map, AUV position estimates were improved relative to the onboard extended Kalman filter (EKF) estimates by using a post-processing EKF and an acausal smoothing algorithm. The mean errors of the onboard EKF and post-processing system were 1.6 and 1.38 meters measured against AUV reference positions provided by an independent acoustic tracking system. The AUV magnetic measurements were improved by over an order of magnitude in post-processing using a magnetometer calibration model and frequency-domain filters such that the post-processed field deviation measurements had an RMS error of 5-10 nT.

Magnetic signature measurement performance was verified by measuring the magnetic signatures of several known magnetic sources: one source was mounted inside a fixed underwater buoy and the other was mounted to the bow of a moving surface vessel. The measured field deviations were compared with predicted field deviations based on a dipole model of the magnetic sources. Errors between measured and predicted fields were generally greatest near the dipole with a maximum magnitude of ~50-200 nT for a given AUV measurement mission, depending on the magnet and mission details.

The magnetic measurement system performance was also quantified using an error propagation which modeled the total error in a measurement of the magnetic field at a point relative to the magnetic source as a function of AUV position, position uncertainty, magnetometer measurement uncertainty, and known local magnetic field characteristics. The actual measurement errors matched the errors predicted by this uncertainty propagation fairly well.

Acknowledgements

I would like to sincerely thank my advisor, Dr. Michael Anderson, for all of his guidance. He was willing to accept me into the graduate Mechanical Engineering program even though I had no formal engineering background, and was then willing to spend the next two years bringing me up to speed on new subjects and bits of engineering-speak and suggesting valuable classes for me to take in order to learn as much as possible in the short time I had. Dr. Anderson cares deeply about providing a quality education for his students: thank you for staying true to that vision.

I would also like to acknowledge the support of the Office of Naval Research through their grant *Electromagnetic Signature Assessment System Using Multiple Autonomous Underwater Vehicles (AUVs)- Phase III*", ONR N00014-10-1-0883, which provided the fiscal resources and expertise that allowed our group to accomplish this project. Additionally I am grateful for the hard work and assistance of everyone on our team, including professors Dean Edwards, Eric Wolbrecht, Terence Soule, and James Frenzel, postdoctoral researcher John Canning, researcher Thomas Bean, Doug Odell of the Office of Naval Research at Bayview, graduate students Jordan Stringfield and Benjamin Armstrong, and of course our undergraduate students Josh Plumb, Ben Wilson, Bryce Gill, and John Feusi, who put in many hours dealing with and improving our data and code.

Table of Contents

Authorization to Submit Thesis	ii
Abstract	iii
Acknowledgements	iv
Table of Contents	v
List of Figures.....	viii
List of Tables.....	ix
Chapter 1: Introduction.....	1
Program Goals	1
AUV Capabilities	2
Prior Work	2
Chapter 2: Navigation Methods	4
AUV Navigation Overview	4
Fleet Formations.....	6
Surface Vessel Navigation	7
Chapter 3: Position Estimation Methods	9
Overview.....	9
Post-processing Long Baseline Filter Model.....	10
Rauch Tung Striebel Smoother	12
Chapter 4: Magnetic Measurement Methods.....	14
Magnetometers.....	14
Voltage Divider	14
Data Acquisition Unit.....	15
Magnets.....	15
Chapter 5: Magnetic Post-processing Methods.....	17

Magnetic Source Modeling	17
Magnetic Signal Filtering	21
Magnetometer Calibration.....	22
Calibration Data Acquisition.....	23
In-Situ Calibration Data Acquisition	24
Land Calibration Data Acquisition	25
Calibration Coefficient Optimization Algorithm.....	27
Chapter 6: Magnetic Results	29
Signal De-spiking and Filtering Results.....	29
In-Situ Calibration Results	30
Land Calibration Results	31
Chapter 7: Magnetic Signature Mapping Results.....	36
Fixed Magnetic Source Map.....	36
Surface Vessel Field Map.....	38
Error Propagation Theory.....	41
Error Propagation Results: Surface Vessel Pass	44
Error Propagation Results: Buoy Pass	45
General Error Propagations.....	47
Error Budget and Significance of Accuracy for Measurements.....	48
Chapter 8: Conclusions.....	49
Project Status	49
Future Research.....	49
References.....	51
Appendices	55
Appendix 1: Log Structure Contents.....	55

Appendix 2: Summary of MATLAB Code for Operations on AUV Data 66

Appendix 3: Extended Kalman Filter Theory 69

Appendix 4: Rauch-Tung-Striebel Smoother Theory 71

List of Figures

Figure 1. Surface vessel magnetic signature measurement by AUV fleet.	2
Figure 2. University of Idaho AUV.	3
Figure 3. Bayview navigation range.....	5
Figure 4. Navigation of surface vessel during magnetic signature measurements.	8
Figure 5. Post-processing EKF AUV positions and RTS smoothed AUV positions.	13
Figure 6. Magnetometer voltage divider.	15
Figure 7. Buoy dipole magnetic deviation isosurfaces.	18
Figure 8. Boat dipole magnetic deviation isosurfaces.....	19
Figure 9. Single AUV buoy pass.	21
Figure 10. Non-orthogonal magnetometer axes.....	22
Figure 11. Overhead view of AUV positions during in-situ calibration.	25
Figure 12. Partial thin shell acquired during in-situ calibration.	25
Figure 13. Non-magnetic calibration apparatus holding AUV during land calibration.	27
Figure 14. Comparison of raw, filtered, and calibrated magnetic data.	30
Figure 15. Pre- and post-calibration magnetic field acquired during calibration.	33
Figure 16. Thin shell acquired during land calibration.	35
Figure 17. Buoy field map surface using topside positions.....	37
Figure 18. Buoy field measurements with both topside and post-processing EKF positions.	38
Figure 19. Unknown magnetic source on surface vessel	39
Figure 20. Surface vessel field map surface using post-processing EKF positions	40
Figure 21. Surface vessel field measurements using topside and post-processing EKF positions.....	41
Figure 22. Error propagation of surface vessel pass by single AUV.	45
Figure 23. Error propagation of buoy pass by single AUV.....	46
Figure 24. Error propagation of buoy pass by single AUV.....	47

List of Tables

Table 1. AUV Navigation Performance.....	13
Table 2. In-Situ Magnetometer Calibration Coefficients.....	31
Table 3. Land Magnetometer Calibration Coefficients	32

Chapter 1: Introduction

Program Goals

The research described in this document was performed as part of the University of Idaho AUV research program under the ONR N00014-10-1-0883 grant. The overarching goal of this program is to assist in the protection of U.S. surface naval vessels from mines in hostile waters.

Ever since the First World War, mines have been a large threat to naval surface vessels, responsible for sinking or damaging more than 3200 vessels. These threats can persist unnoticed for decades, ready to detonate on observation of the right signal [1]. Advanced mines may use a combination of acoustic, pressure, and other sensors to determine that an enemy surface vessel is present, but many mines may be triggered by a disturbance in the background geomagnetic field [1]. This is a difficult threat to mitigate in naval vessels, since they are generally made out of ferrous alloys which have induced magnetic fields and possibly permanent magnetization. Vessels may be degaussed before navigating to a forward area in order to remove much of the permanent magnetization, but after being degaussed, the vessel can become re-magnetized as it travels to a forward operating area within the geomagnetic field. Since the induced ship field is a function of the geomagnetic field, itself a function of ship location [2], it is useful to measure this field at a forward area.

This measurement is helpful both to determine if the magnetic signature is dangerously large, and on certain ships, to reduce the total magnetic signature using onboard degaussing coils to counteract the measured ship field [2]. This magnetic signature assessment can be accomplished by setting up a fixed magnetic measurement range at the forward deployment area, but a more flexible and rapid solution would be useful. The AUV project is one approach to solving this problem, providing a fleet of AUVs that can simultaneously navigate under the ship and measure its magnetic field. Figure 1 contains a schematic view of a surface vessel pass in which an AUV fleet and the surface vessel navigate past each other on opposite headings. This pass configuration was chosen to minimize the effect of potential surface vessel propeller wash on AUV navigation performance: the surface vessel propeller wash is expected to have the largest effect after the measurement is complete and the surface vessel has passed above the AUV fleet. The fleet measurement such as the

one illustrated in Fig. 1 are referred to as fleet passes, and may be repeated at varying surface vessel orientations. In each pass the AUVs have a uniform lateral spacing in order to measure a large region of surface vessel fields. The requirements for magnetic signature measurement include a precision of 100 nT over a range of $\pm 100,000$ nT, although 25 nT precision was targeted for the entire magnetometer/AUV system. The position of each magnetic measurement should also be known to an accuracy of 1 meter relative to the surface vessel.

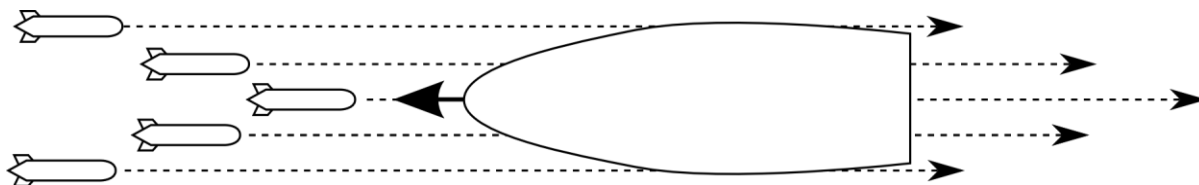


Figure 1. Schematic of surface vessel magnetic signature measurement by an AUV fleet.

AUV Capabilities

The AUVs used to accomplish these magnetic signature measurements are the culmination of several years of design at the University of Idaho, and were originally based on a design by Stilwell et al. at the Virginia Polytechnic Institute and State University [3]. Figure 2 contains a photograph of a typical AUV with annotations identifying several key components. The vehicles developed for this work are about 102 cm long and 10 cm in diameter. Each vehicle is equipped with a six degree of freedom inertial measurement unit, a triaxial fluxgate vector magnetometer, and an acoustic modem used for tracking and communication, along with a number of additional sensors. Each magnetometer is mounted in a separate tube with a length of about 24 cm and a diameter of 5 cm. This tube is mounted parallel to the AUV body. A set of voltage dividers reduces the magnetometer output voltage to a range suitable for the data acquisition unit. Most of the significant navigation and magnetic data is recorded onboard the AUVs for later analysis.

Prior Work

Previous work by other AUV research groups has focused primarily on AUV navigation and localization techniques, although magnetic measurements have been performed using a single AUV to navigate on the water surface around a surface vessel in order to measure the vessel's magnetic signature and model the magnetization of the surface vessel. Previous magnetic work done by the University of Idaho has demonstrated magnetic mapping of unknown sources near a lake shore [4].

A magnetometer RMS error of 21 nT was observed during straight navigation in a clean magnetic field [5], but an improvement would aid magnetic signature mapping. The author's own publications include mapping of the fixed buoy magnet and preliminary magnetometer calibration results [6].

Regarding navigation, much work has been done on AUV localization relative to a single transponder [7] [8], localization using cooperative AUVs [9], and localization relative to fixed transponder arrays [10]. Previous work at the University of Idaho demonstrated AUV onboard EKF position estimation with an accuracy of ~ 1.8 m using a fixed transponder array described in Chapter 2 [5]. Additionally, preliminary testing has been completed for a navigation algorithm and a portable acoustic transponder apparatus designed to allow simultaneous navigation of multiple AUVs relative to a moving surface vessel [11]. A new post-processing filter has been developed and used to provide improvements in position estimates for AUV passes described in this document [12].

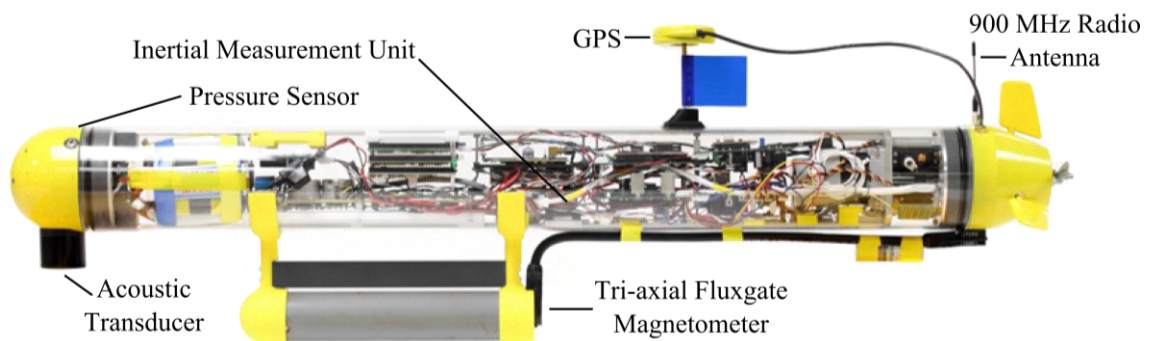


Figure 2. University of Idaho autonomous underwater vehicle (AUV).

Chapter 2: Navigation Methods

AUV Navigation Overview

The AUVs are field tested at the acoustic research detachment (ARD) of the naval surface warfare center (NSWC) located on Lake Pend Oreille, ID. The testing facility has been equipped with two bottom mounted transponder ranges; one located in shallow water and one located at a depth of approximately 200 meters, hereafter termed the deep water range. Both transponder ranges have a set of four to five transponders arranged in a widely spaced geometry designed for AUV tracking accuracy inside of the transponder range. The approximately circular set of transponders comprising the deep water range is shown in Figure 3. The transponders intermittently broadcast messages to the AUVs at known time intervals. Since the AUVs use clocks synchronized with the transponders, they can determine ranges to the transponders by recording the time of arrival of the transponder broadcasts. Thus this approach is termed synchronous navigation [13]. This range information is the key source of AUV position data during underwater operation, and due to the large transponder geometry relative to AUV paths this transponder configuration is also termed long-baseline navigation (LBL). This synchronous LBL implementation is described in much greater detail in [14].

Several other AUV localization techniques have been tested at the deepwater range, such as moving short baseline navigation (MSBL) based on the work by [15], [16], and [17]. In the approach used by this research group, a pair of transponders mounted to a moving surface vessel broadcast messages containing information regarding surface vessel location at known intervals. The broadcast message contents provide information regarding surface vessel location and the broadcast arrival times provide information regarding AUV location relative to the surface vessel. The MSBL navigation approach is described in [11].

Synchronous LBL navigation was the only localization technique used to provide transponder ranges for onboard AUV localization for the work in this text. All the magnetic experiments described in this document were carried out using the deep water tracking range far from any undesired objects such as the barge. Only the deep water range provides the magnetically clean environment required for accurate magnetic signature assessments, as earlier surveys of the shallow water range detected a background field that was not spatially uniform [18].

The bottom-mounted transponders of the deep water range also recorded intermittent AUV acoustic pings and used them to create an independent set of AUV positions, referred to and treated as AUV reference positions. The reference position calculations contained a more complex procedure to find AUV ranges and location than other approaches, for instance including the measured variations in speed of sound as a function of depth, and the reference positions provide the most accurate measurements of AUV positions. The reference position system of the shallow water range has demonstrated accuracies of up to 0.01 meters depending on measurement method [19]. The transponders in the deep water range are arranged in an approximately circular pattern with a diameter of over 300 meters, so that the ranges to the AUVs during testing are generally much larger than ranges from the shallow water tracking system. Thus, the deep water reference position system is less accurate, with a measured accuracy relative to differential GPS surface vessel position measurements of 0.01-0.6 meters, depending on measurement method.

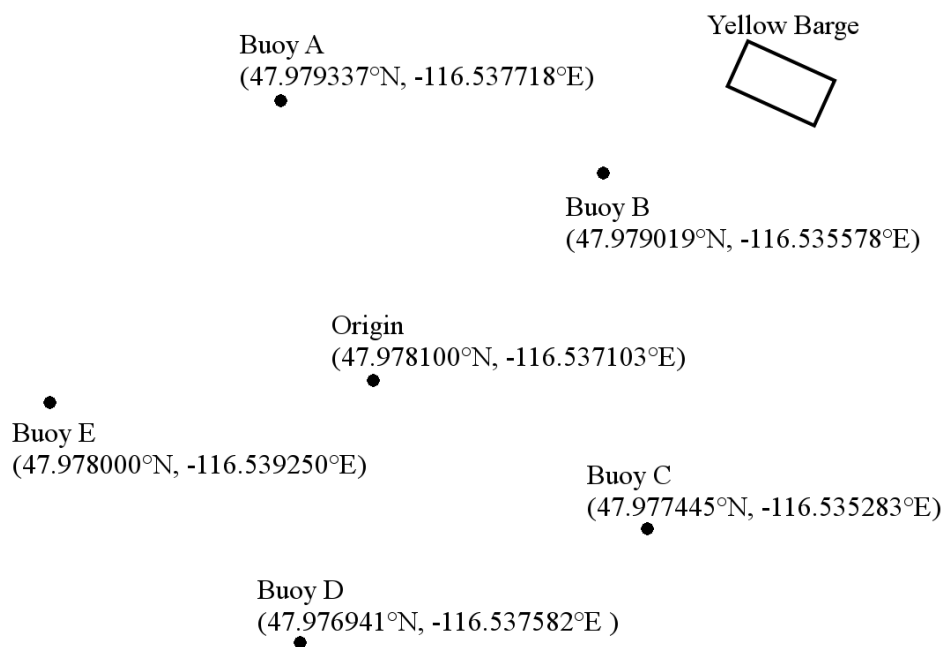


Figure 3. Bayview navigation range: latitude and longitude of transponders fixed to lake floor.

The global coordinate system for objects at the deep water range is specified in terms of latitude and longitude, as in Figure 3. Since latitude and longitude are computationally cumbersome, all local positions, including all positions in this text, were specified in terms of north, east, and height positions relative to the local coordinate system origin in the center of Fig. 3. The AUV

positions were initialized using GPS latitude and longitude measurements, but AUV and surface vessel positions were generally stored and processed as North and East coordinates relative to the local coordinate system origin.

The AUVs follow a predefined set of straight paths between waypoints using the path following algorithm described in [5]. During the magnet pass missions described in this paper, the waypoint paths generally formed a straight path facing East or West. A proportional-integral-derivative (PID) feedback controller implemented on a distributed control architecture described in [20] kept the AUV close to the desired course using an estimate of the AUV state provided by an extended Kalman filter (EKF). The onboard EKF combined onboard sensor information such as pressure measurements or propeller rotation rate measurements with acoustic range information from the long baseline (LBL) transponder array to accurately estimate the state of the AUV (North, East, speed, heading, and heading bias). A heading bias state has been added in order to improve state estimation performance in the presence of a magnetic gradient, as described in [20]. The work described in this text did not involve modification or analysis of the onboard Kalman filter.

Fleet Formations

The AUVs were designed to be operated simultaneously using the Kalman filtering, path following, and waypoint missions described above. When operated as a fleet, one AUV was designated the leader and the others the followers. The leader sent out an intermittent leader broadcast describing its current progress along the waypoint paths, and the other AUVs adjusted their positions relative to the leader AUV in order to maintain the desired fleet spacing. The leader broadcast was transmitted using the acoustic transponder and caused a visible and predictable disturbance in the measured magnetic field.

Various AUV fleet formations were used during this testing, but all specified that the AUVs navigate in parallel paths with a set distance between adjacent paths. During passes termed fixed underwater buoy passes, the AUVs navigated as a fleet above the fixed underwater buoy, reversed heading, and then navigated above the fixed underwater buoy a second time. AUV depths were set to 3, 3.5, or 4 meters and AUV lateral spacing between adjacent AUVs was set to 3 meters. During the first portion of the pass the leader AUV waypoint path passed directly over the fixed buoy source and the two follower AUVs paths were three and six meters south of the leader AUV path.

On the second portion of the pass, the leader AUV waypoint path was six meters north of the fixed buoy and the two follower AUV paths remained three and six meters south of the leader AUV path.

In the case of the moving surface vessel passes, initial tests showed that the AUVs had to be very close to the surface vessel to effectively measure its field, and it was known that the dipole field disturbance isosurfaces under the AUV were approximately bowl-shaped, as described in Chapter 4. Thus the fleet of three AUVs used during surface vessel passes was positioned such that the AUVs would have the highest chance of recording a signature while navigating at a safe distance from the surface vessel and each other. The AUV positioned 0.5 meters north of the surface vessel centerline had a waypoint depth of 4 meters, the AUV positioned 0.5 meters south of the surface vessel centerline had a waypoint depth of 3.5 meters, and the AUV positioned 1.5 meters north of the surface vessel centerline which passed under the center of the surface vessel had a waypoint depth of 3 meters. A fourth AUV position 1.5 meters south of the surface vessel centerline and at a depth of 2.5 meters was planned but never utilized due to problems experienced by the fourth AUV.

Surface Vessel Navigation

During AUV missions intended to measure the magnetic signature of a surface vessel, the surface vessel itself was navigated by an operator along a predefined waypoint path in a heading opposite to the AUV fleet heading. The operator used a computer display indicating the GPS estimate of the surface vessel location and the desired waypoint path to navigate the vessel along the path. During the majority of vessel operations, lateral error between the surface vessel and the desired waypoint path was under 1.5 meters, as shown in Figure 4. Since the differential GPS positions of the surface vessel were available after the run was complete, this error did not impede analysis of the run, but it did prevent the AUVs from navigating precisely under the surface vessel in their desired paths. The figure below shows a characteristic surface vessel waypoint path.

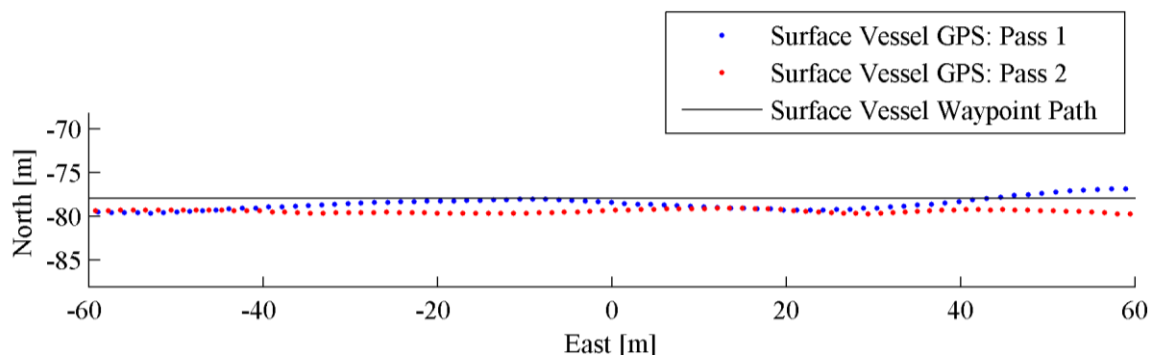


Figure 4. Navigation of surface vessel during magnetic signature measurements by AUV fleet. Surface vessel generally was within 1.5 meters of the waypoint path at -77.92 meters North.

Chapter 3: Position Estimation Methods

Overview

The accuracy on the onboard Kalman filter relative to the ground truth positioning system during typical missions executed at the deep-water range was approximately 1.6 meters. Since this accuracy was not sufficient to meet program requirements, additional post-processing was performed on the AUV data in order to improve the position estimates. This post-processing included two components: the post-processing extended Kalman filter and the post-processing smoothing algorithm.

The post-processing Kalman filter operates on stored AUV data that has been parsed into a standard Log file in MATLAB. The Log structure contains fields for each of the different data types, such as sensor packets, onboard Kalman position solutions, acoustic modem communications, etc. Each field contains a timestamp in seconds past midnight GPST so that events may be correlated in time. To aid in this correlation, the Log also has a chronological event list, allowing one to read through Log data in the same order that it was acquired onboard the AUV.

The Log event list is used by the post-processing EKF as one means of improving position estimation accuracy compared to the onboard EKF. While the onboard EKF is based on the assumption that all measurements take place at 0.25 second intervals, the post-processing EKF has no such limitation and may update the Kalman filter at arbitrary intervals corresponding more closely to measurement times.

A more detailed description of the Log contents and the software used to work with it may be found in Appendix 1 and Appendix 2, respectively. In practice, the Kalman filtering function opened a given Log file, propagated and updated a state estimate for each time increment corresponding to a measurement as listed in the Log event list, and saved the state estimates as an additional field in the Log. The various Kalman filter parameters such as state transition model, measurement model, process and measurement noise covariance, and initialization conditions were generated using a MATLAB script with symbolic variables. A brief description of Kalman filter theory may be found in Appendix 3, and the notation and equations used in this work were based primarily on the Kalman filter derivations and discussions in [21].

Post-processing Long Baseline Filter Model

The EKF used for producing post-processing estimates of AUV position used the following state, as described in more detail in [12]

$$x = [N \quad E \quad s \quad \psi \quad b]^T.$$

In this equation, N represented the North coordinate of the AUV relative to the origin of the local reference frame at the deep water testing area, E represented the East coordinate of the AUV relative to the local reference frame, s represented AUV speed, ψ represented AUV heading, and b represented a heading bias. The measurement was defined as

$$y = [r_1 \quad r_2 \quad r_3 \quad r_4 \quad s_m \quad \psi_m]^T.$$

In this measurement model, r_1 - r_4 were the four transponder ranges, s_m was a speed calculated as a linear function of measured propeller RPM, and ψ_m was the measured heading using an onboard compass separate from the triaxial fluxgate magnetometer. The state update equation was

$$x_k = f_{k-1}(x_{k-1}, u_{k-1}, \omega_{k-1}) = \begin{bmatrix} \Delta t \cdot s \cdot \cos(\psi) + N + \omega_N \\ \Delta t \cdot s \cdot \sin(\psi) + E + \omega_E \\ s + \omega_s \\ \Delta t \cdot \dot{\psi}_m + \psi_m + \omega_\psi \\ b + \omega_b \end{bmatrix}_{k-1}.$$

The discrete time state update equation used to propagate the state estimate from time $k - 1$ over time interval Δt to time k simply modeled the AUV as traveling forward continuously at its current velocity, heading, and rate of heading change. An inertial measurement unit (IMU) input of measured angular rate about the yaw axis, $\dot{\psi}_m$, was used in the model, although this input was not one of the measurements in y . No AUV sideslip was modeled. The terms ω_N , ω_E , ... ω_b were additive process noises for the North, East, speed, heading, and heading bias states. The measurement update equation was

$$\hat{y}_k = h_k(x_k, u_k) = \begin{bmatrix} \sqrt{(N - N_{T1})^2 + (E - E_{T1})^2 + (\Delta Z_{T1})^2} + v_{r1} \\ \sqrt{(N - N_{T2})^2 + (E - E_{T2})^2 + (\Delta Z_{T2})^2} + v_{r2} \\ \sqrt{(N - N_{T3})^2 + (E - E_{T3})^2 + (\Delta Z_{T3})^2} + v_{r3} \\ \sqrt{(N - N_{T4})^2 + (E - E_{T4})^2 + (\Delta Z_{T4})^2} + v_{r4} \\ s + v_s \\ \psi + b + v_\psi \end{bmatrix}_k$$

The measurement update equation was used to determine the expected measurement given a particular state. The update equation included terms for the four ranges from the four fixed transponders, the propeller RPM measurement, and the angular rate measurement from the IMU axis corresponding to AUV yaw. The fixed transponder locations were denoted by $N_{T1}, E_{T1}, \dots, N_{T4}, E_{T4}$. The differences in elevation between the AUV elevation as determined by the pressure sensor and the fixed transponders were denoted by $\Delta Z_{T1} \dots \Delta Z_{T4}$. The terms $v_{r1}, v_{r2}, \dots, v_s, v_\psi$ were additive measurement noises for the first transponder range, second transponder range, third transponder range, fourth transponder range, speed measurement, and heading measurement, respectively.

The covariance matrices used by the EKF to model process and measurement noise were determined by optimization of the covariance numbers in a MATLAB function to minimize post-processing EKF error relative to the reference position system over a wide variety of typical AUV navigation operations. The optimization function constrained the non-diagonal terms of the noise matrices to be zero. The following coefficients determined by optimization were used for all post-processing EKF position estimates in this text.

$$R = \begin{bmatrix} v_{r1} & 0 & 0 & 0 & 0 & 0 \\ 0 & v_{r2} & 0 & 0 & 0 & 0 \\ 0 & 0 & v_{r3} & 0 & 0 & 0 \\ 0 & 0 & 0 & v_{r4} & 0 & 0 \\ 0 & 0 & 0 & 0 & v_s & 0 \\ 0 & 0 & 0 & 0 & 0 & v_\psi \end{bmatrix}$$

$$= \begin{bmatrix} (1.5413 \text{ m})^2 & 0 & 0 & 0 & 0 & 0 \\ 0 & (1.5413 \text{ m})^2 & 0 & 0 & 0 & 0 \\ 0 & 0 & (1.5413 \text{ m})^2 & 0 & 0 & 0 \\ 0 & 0 & 0 & (1.5413 \text{ m})^2 & 0 & 0 \\ 0 & 0 & 0 & 0 & (0.3023 \frac{\text{m}}{\text{s}})^2 & 0 \\ 0 & 0 & 0 & 0 & 0 & (0.0386 \text{ radians})^2 \end{bmatrix}$$

$$\begin{aligned}
Q &= \begin{bmatrix} \omega_N & 0 & 0 & 0 & 0 \\ 0 & \omega_E & 0 & 0 & 0 \\ 0 & 0 & \omega_S & 0 & 0 \\ 0 & 0 & 0 & \omega_\psi & 0 \\ 0 & 0 & 0 & 0 & \omega_b \end{bmatrix} = \\
&= \begin{bmatrix} (0.0033 \text{ m})^2 & 0 & 0 & 0 & 0 \\ 0 & (0.0033 \text{ m})^2 & 0 & 0 & 0 \\ 0 & 0 & (0.0016 \text{ m})^2 & 0 & 0 \\ 0 & 0 & 0 & (0.2916 \text{ radians})^2 & 0 \\ 0 & 0 & 0 & 0 & (0.0067 \text{ radians})^2 \end{bmatrix}
\end{aligned}$$

As an additional advantage over the onboard EKF, the post-processing EKF was able to save many of the intermediate EKF variables not stored by the onboard EKF that were necessary for certain types of data smoothing.

Rauch Tung Striebel Smoother

The Rauch Tung Striebel (RTS) smoother described in this work used the original work by [22]. The state update and measurement equations are assumed to be linear and the time interval between updates is supposed to be uniform. In practice, the state and measurement equations are not linear and the time interval is not uniform: due to vagaries in the AUV recording hardware and software, sensor data is recorded at unpredictable time intervals. Nevertheless, the RTS smoother successfully improves the position estimates provided by the post-processing EKF. A brief description of RTS smoother theory may be found in Appendix 4.

A set of typical AUV positions provided by the post-processing EKF and RTS smoother and reference positions are shown in Fig. 5. The advantages of the acausal RTS smoother are apparent, especially in the lower run in Fig. 5. The AUV navigated on an East heading in both runs. Discontinuities in the post-processed EKF positions are visible at those times when the EKF received new information about AUV location from buoy ranges and adjusted its position estimate accordingly. Since the EKF was causal, it could not use information regarding future ranges to adjust its present state. The acausal RTS smoother, on the other hand, was able to use information saved by the post-processing EKF to eliminate the AUV position discontinuities and improve the position estimate. The majority of the improved position estimation accuracy achieved by post-processing was due to the RTS smoother rather than the post-processing EKF, as seen in Table 1.

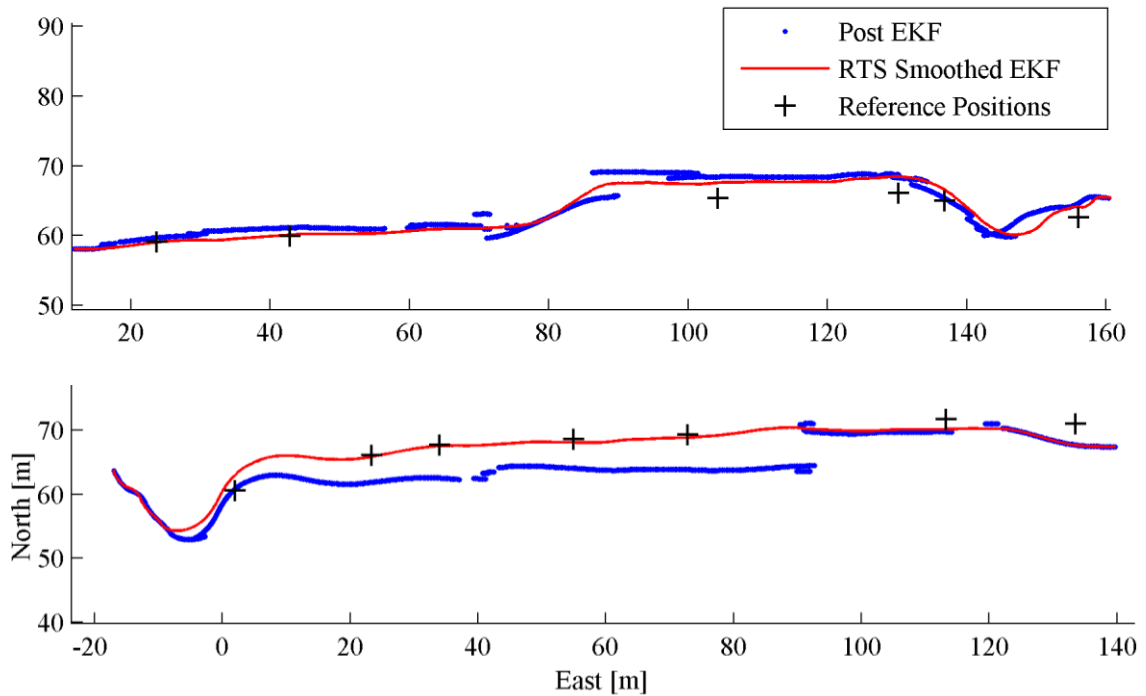


Figure 5. Post-processing EKF AUV position estimates and improved RTS smoothed AUV position estimates for two characteristic AUV runs.

The post-processing EKF and RTS smoother provided measurable improvements in AUV position error relative to reference positions when compared to the onboard filter, with the combination of post-processing EKF and RTS smoother displaying the best performance. Further information on the post-processing EKF and RTS smoother may be found in [12].

Table 1. AUV Navigation Performance.

<i>Method</i>	Onboard EKF	Post EKF	Smoothed EKF	Reference Tracking System**
RMS error [m]	1.60	1.53	1.38	0.01-0.6

** AUV reference tracking system error statistics relative to true positions [19].

Chapter 4: Magnetic Measurement Methods

Magnetometers

The magnetometers used for this work were Billingsley TFM100G4-UHW triaxial fluxgate magnetometers. Each magnetometer has three independent fluxgates designed to measure magnetic field vector components along three orthogonal axes. Exhaustive details of the triaxial fluxgate magnetometer construction and operation for the Ørsted satellite mission may be found in [23], and a summary and comparison of triaxial fluxgate magnetometer capabilities with other classes of magnetometer may be found in [24]. Manufacturer specifications for the TFM100G4-UHW describe the field range as $\pm 100,000$ nT, the sensitivity as 100 μV per nT, and the linearity of the sensor as 0.0035% of full scale, or 3.5 nT [25]. Each magnetometer was placed in a separate tube with a length of 23.6 cm and a diameter of 4.83 cm which was mounted below and parallel to the AUV hull, as shown in Fig. 2. The three single-ended magnetometer signals, one for each fluxgate, were reduced in voltage using a set of resistor dividers and then provided to the data acquisition unit (DAQ) onboard the digital signal processor (DSP), which then stored the data in binary form on a removable SD card for later analysis.

Voltage Divider

Since the voltage output of the AUV magnetometer was ± 10 V, but the analog to digital converter (ADC) used on the data acquisition unit (DAQ) had a permitted voltage range of ± 2.5 volts, a set of voltage dividers was used to reduce the magnetometer output voltages representing a signal for each fluxgate V_a, V_b, V_c to voltages V_d, V_e, V_f respectively that were suitable for the ADC. The voltage divider resistors R_2 shown in Fig. 6 had a lower resistance than would otherwise be desired due to anomalous behavior of the DAQ when used with a high resistance voltage divider. Throughout this document the voltage divider was assumed to reduce the voltage on each axis by a factor of exactly 8, although this may not have been the case in practice. If the nominal resistances listed for the voltage divider in several pieces of documentation are correct, the voltage divider may have reduced the voltage by a factor of 8.14.

Data Acquisition Unit

The magnetic signal was converted from an analog format to a digital format using the D.SignT D.module.AD7722 analog to digital converter (ADC) expansion board in conjunction with the D.SignT D.module.6713 DSP board. The ADC used delta-sigma modulation with a 16-bit resolution and fully differential signaling on the analog inputs, which had an input impedance of $2.5\text{M}\Omega$. The 16-bit quantization limited to the ADC to a resolution of 3.04 nT per least significant bit. Since the magnetometer signal was single-ended, one half of the differential signal inputs were connected to a common ground. This DSP was initially chosen for its ability to record acoustic data at a high sample rate of up to 200 kHz . Although a high sample rate was not required for magnetic measurements, the ADC was configured to record three independent magnetometer channels at 16.67 kHz onto a SD card located on the DSP. This data was retrieved after testing and combined with other data from the same tests within a MATLAB Log structure after appropriate data filtering, sub-sampling, and magnetometer calibration algorithms were applied.

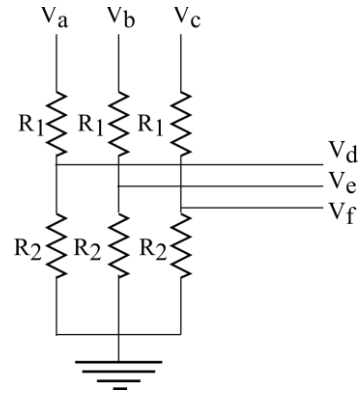


Figure 6. Magnetometer voltage divider matches magnetometer output voltage range to DAQ input voltage range. $R1 \approx 100\text{K}\Omega$, $R2 \approx 14\text{K}\Omega$. Signal voltage reduced by a factor of ~ 8 .

Magnets

Two known magnetic sources were used for magnetic measurements by AUVs. First, a fixed underwater buoy containing a cluster of four magnets with a combined dipole moment of 448 Am^2 was used to verify AUV magnetic measurement performance near a known magnetic source in a clean magnetic environment. The magnet was mounted such that the dipole was oriented vertically in order to eliminate the dependence of the magnetic field on potential buoy rotation about its yaw axis. The fixed underwater buoy was placed at the (North, East) coordinates of $(-70.81, -45.75)$ meters with respect to the deep-water coordinate system origin shown in Fig. 3. The depth of the underwater buoy was a function of water level in the lake: at a characteristic water surface level of 626.52 meters above sea level, the depth of the dipole was 9.11 meters. Calculations regarding the expected field produced by the fixed buoy source took into account variations in the lake surface

level from this characteristic surface level as a constant deviation for a given day of testing. AUV operations in the vicinity of this fixed underwater magnet are referred to as buoy passes.

Second, a single magnet with a dipole moment of 135 Am^2 was mounted to a differential GPS mast onboard the surface vessel to verify system performance for a moving vessel. This magnet was also mounted vertically to eliminate dependence of the magnetic field on surface vessel heading. The horizontal coordinates of this magnet were recorded by the dGPS system for later analysis, while the height of the magnet above the water depended on the weight in the surface vessel and the day of testing: in general it was approximately 0.3 meters above the surface of the water. AUV operations in the vicinity of this magnet are referred to as surface vessel passes.

Chapter 5: Magnetic Post-processing Methods

Magnetic Source Modeling

Since the AUV magnetic measurements frequently involved measurement of known magnetic sources for testing, modeling the expected magnetic field measurements permitted an analysis of measurement system performance. As a first-order approach, the background geomagnetic field was considered a static uniform field and each known magnetic source was treated as an ideal dipole.

The background geomagnetic field was approximated by using the World Magnetic Model 2010 to find predicted field for the latitude, longitude, and elevation of the deep-water testing range for a date approximate to the date of testing [26]. The geomagnetic field components predicted by this model were $\vec{B}_g = [4853, 17571, -52287]$ nT in the (East, North, Vertical) axes respectively.

The total predicted magnetic field \vec{B} was determined for a given AUV position by adding the predicted geomagnetic field to any predicted dipole fields \vec{B}_{m_i} due to i magnets using the principle of superposition.

$$\vec{B} = \vec{B}_g + \sum_i \vec{B}_{m_i}$$

The field produced by each magnet at a specific location in space is found using the classical dipole model [27]

$$\vec{B}_m = \frac{\mu_0}{4\pi r^3} (3(\vec{m} \cdot \hat{r})\hat{r} - \vec{m})$$

$$\mu_0 = 4\pi \cdot 10^{-7} \frac{V \cdot s}{A \cdot m}$$

Several variables are based on the vector \vec{r} from the magnet position to the position of the observer or magnetometer,

$$\vec{r} = [x \quad y \quad z]^T - [x_m \quad y_m \quad z_m]^T, \hat{r} = \frac{\vec{r}}{|\vec{r}|}, r = |\vec{r}|.$$

The magnet dipole moment \vec{m} may be broken into vector components, and since both magnets were mounted with vertical dipole orientations,

$$\vec{m} = [0 \quad 0 \quad m_z]^T.$$

The following figure, Fig. 7, illustrates the expected field disturbance within the background geomagnetic field due to the fixed buoy magnet. The geomagnetic field vectors are illustrated as red arrows. When added to the dipole field, the total field deviation from the background geomagnetic field has the lobed shapes shown in the figure. In the toroidal regions where the dipole field adds to the geomagnetic field, the field deviation is positive. In the polar regions where the dipole field subtracts from the geomagnetic field, the deviation is negative. Thus the shaded isosurfaces of constant deviation represent either a positive or a negative deviation in background field magnitude. Since the buoy is mounted at ~ 9 meters depth and the AUVs generally navigate near ~ 2 meters depth, the blue box indicates the expected AUV navigation range and the expected disturbance measurement of between -100 and -400 nT.

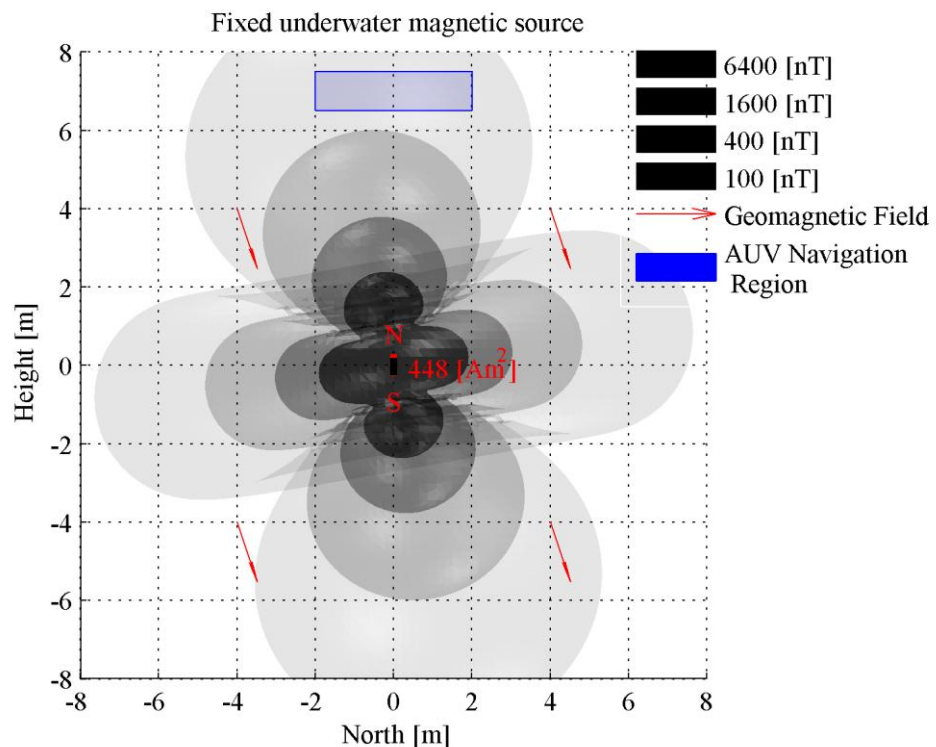


Figure 7. Buoy dipole predicted magnetic deviation isosurfaces in geomagnetic background field. The blue box indicates expected AUV fleet navigation region relative to fixed magnet. The toroidal isosurfaces are positive magnitude deviations while the polar isosurfaces are negative magnitude deviations.

Figure 8 illustrates similar isosurfaces for the surface vessel magnet within the same geomagnetic background field. In both Fig. 7 and Fig. 8 the magnet's north and south poles are illustrated in the figures as the 'N' and 'S' above a vertical red and black bar representing the magnet. In Fig. 8 the surface vessel magnet has a much smaller dipole moment, so the deviation isosurfaces are much smaller than the buoy magnet. The blue box in this figure indicates the expected navigation region of the AUVs underneath the surface vessel during a surface vessel pass region. The grey surfaces within the blue box are an indication that the magnetic field deviations measured during a surface vessel pass would be between -100 and -1600 nT, a much larger range than the expected deviations due to the fixed buoy.

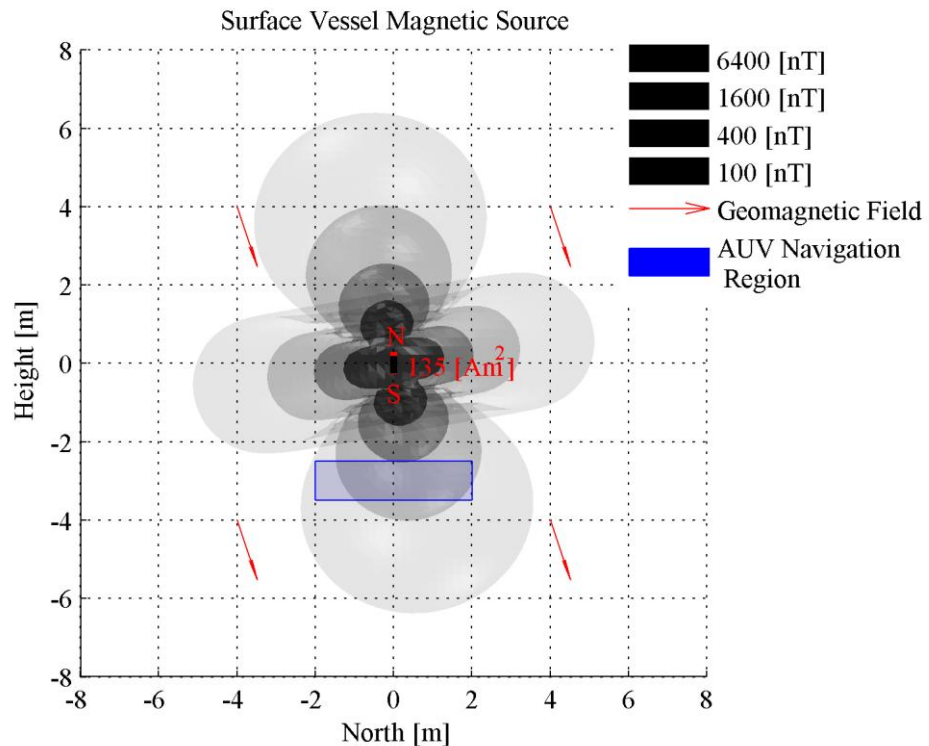


Figure 8. Boat dipole magnetic deviation isosurfaces in geomagnetic background field. The blue box indicates expected AUV fleet navigation region relative to the surface vessel. The toroidal isosurfaces are positive magnitude deviations while the polar isosurfaces are negative.

In general, the fields predicted using the dipole model for the fixed underwater buoy matched the fields measured by the AUV well, as shown in Fig. 9 for a characteristic measurement. In this figure a single AUV navigated above the fixed buoy magnet, reversed course, and then passed the magnet a second time. The predicted field deviations shown here were found using the dipole model at linearly interpolated reference positions: the test was intended to demonstrate

magnetometer measurement and dipole modeling accuracy rather than EKF accuracy. The error between the predicted and measured magnetic field was generally greatest where the predicted dipole field is strongest.

Two additional observations are important. First, the approximate measured field deviation is found by subtracting the mean of the measured field from each magnetic field measurement. However, the mean of the measured field is lower than the actual geomagnetic background field due to the measurements in the vicinity of the magnet. An additional constant value is subtracted from the approximate measured field deviation in order to align measured magnetic field deviations away from any magnetic sources with the correct value of 0 nT. Since this correction value depended on the number of measurements and the AUV locations relative to the magnet, it was manually determined for all magnetic deviation figures in this document.

Second, the measured magnetic field changed rapidly halfway through the AUV mission in the region of Fig. 9 in between the two dipole measurements. This magnetic field change occurred when the AUV reversed its heading in a magnetically clean environment. While the magnetometer calibration procedure removes nearly all of the orientation-dependent magnetometer errors in the original signal, it does not remove them completely. This may be caused either by nonlinearities in the magnetometer which cannot be accounted for by the linear model, by a time-dependence of the magnetometer model, or by other factors such as the induced field of the AUV.

As the dipole model matched experimental data well, and the dipole moments of the magnets were the only specification data included with the magnets from NSW Carderock, applying a higher order model would have been infeasible and of little benefit.

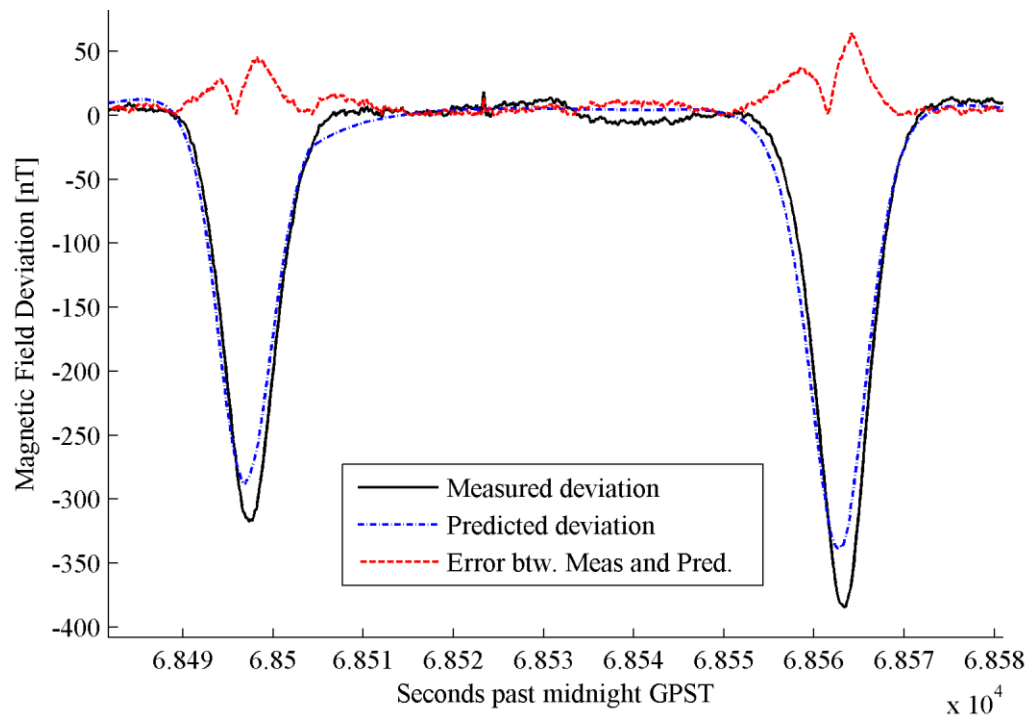


Figure 9. Single AUV buoy pass demonstrates dipole model accuracy. Reference positions were used to find the predicted magnetic deviation.

Magnetic Signal Filtering

The raw magnetic data recorded at 16.67 kHz could not be effectively analyzed directly due to signal noise and the very large data file sizes. The triaxial magnetometer voltages recorded by each AUV run were filtered and decimated using MATLAB functions before being saved in the MATLAB Log file according to the following procedure. First the signals were processed by a custom de-pinging algorithm which removed the sudden spikes in magnetic field caused by the brief AUV navigation pings used by the reference tracking system to find AUV positions. Several of these navigation pings may be seen in the unfiltered magnetic data in Fig. 14. The de-pinging algorithm used a highpass filter to isolate the high frequency component of the signal and then removed points with a magnitude greater than four times the standard deviation of the highpass filtered signal. The removed points were replaced with a linear interpolation of adjacent points. This algorithm successfully removed noisy data acquired during navigation pings without removing excessive amounts of genuine data.

The magnetometer signal was then sequentially filtered and subsampled three times using a 6th order Chebyshev Type II lowpass filters with a stop-band ripple of -20 dB. During the first

operation, the signal was lowpass filtered to a stop-band of 333 Hz and then subsampled at 1000 Hz. In the second operation, the signal was lowpass filtered to a stop-band frequency of 33.3 Hz and then subsampled at 100 Hz. Finally the signal was lowpass filtered to a stop-band frequency of 3.33 Hz and subsampled at 10 Hz. The de-pinged, lowpass filtered, and down-sampled magnetometer voltages recorded by the DSP were then stored in the Log file to be subsequently converted to magnetic fields by application of the magnetometer calibration model.

Magnetometer Calibration

The sensor model used to calibrate the magnetometers approximated the three nearly orthogonal magnetometer fluxgates as independent linear sensors using nine calibration coefficients, following the model described in [28].

Three coefficients, α , β , and γ , described the angles between the sensor axes as shown in Fig. 10, and for each axis i , two coefficients, a_i and b_i , described the gain and offset coefficients to transform a sensor voltage to a magnetic field strength.

According to this model, the measured magnetic field component along a fluxgate axis B_i was a linear function of the fluxgate voltage V_i : $B_i = a_i V_i + b_i$.

Given the manufacturer's specification for

magnetometer nonlinearity of 3.5 nT, this was a

reasonable assumption: additional analysis of fluxgate nonlinearities and transverse effects may be

found in [29]. In more detail, the true magnetic field \vec{B} represented by the three orthogonal

magnetic field components $[B_x \ B_y \ B_z]^T$ may be found from the magnetometer voltages

$[V_d \ V_e \ V_f]^T$ along the three slightly non-orthogonal fluxgate axes $\{\hat{d}, \hat{e}, \hat{f}\}$ as measured by the

DAQ and the following model, a linear abbreviation of the cubic model in [30]

$$\vec{B}(\alpha, \beta, \gamma, a_d, a_e, a_f, b_d, b_e, b_f) = \begin{bmatrix} B_x \\ B_y \\ B_z \end{bmatrix} = \Psi[A * V + b]$$

where the orthogonalization matrix Ψ and the gain matrix A

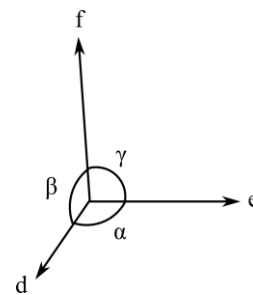


Figure 10. Non-orthogonal magnetometer axes $\{\hat{d}, \hat{e}, \hat{f}\}$ and angles between axes.

$$\Psi = \begin{bmatrix} 1 & 0 & 0 \\ \cos(\alpha) & \sin(\alpha) & 0 \\ \cos(\gamma) & \cos(\gamma) & \sqrt{1 - \cos^2(\beta) - \cos^2(\gamma)} \end{bmatrix}^{-1}, A = \begin{bmatrix} a_d & 0 & 0 \\ 0 & a_e & 0 \\ 0 & 0 & a_f \end{bmatrix}.$$

The sensor input voltages and offsets, respectively, are

$$V = \begin{bmatrix} V_d \\ V_e \\ V_f \end{bmatrix}, b = \begin{bmatrix} b_d \\ b_e \\ b_f \end{bmatrix}.$$

Assuming a perfect sensor with orthogonal axes and sensitivity that matched manufacturer's specifications, $\alpha = \beta = \gamma = \frac{\pi}{2}$ radians, and for each axis i , $a_i = 80000 \frac{\text{nT}}{\text{V}}$, $b_i = 0$ nT. In order to determine the particular calibration coefficients for a magnetic measurement system, including ADC, voltage divider, and magnetometer, a set of magnetic measurements at varying orientations with respect to the total magnetic field vector was taken in a known field.

Calibration Data Acquisition

Two methods of obtaining calibration data used to determine the calibration coefficients described above have been tested. The magnetic signal filtering procedure described above was applied to the calibration data before it was used, with two exceptions. First, the custom de-pinging algorithm was not required as no AUV navigation pings were sent during the calibration data acquisition. Second, the final decimation step was not applied. This increased the number of data points available during the calibration compared to typical AUV data: the calibration data was lowpass filtered to 33.3 Hz and stored at 100 Hz.

In both calibration data acquisition methods the AUV was rotated through a range of orientations within the nearly constant magnitude background geomagnetic field while the onboard magnetometer recorded the measured field. As the orientation range of the AUV increased towards including all solid angles, the magnetic field vectors recorded by the magnetometer approached a roughly spherical shape or shell within the magnetometer reference frame. Thus this calibration approach is termed thin shell calibration following the convention of [31]. This general approach has been used successfully for pre-flight magnetometer calibrations of a triaxial fluxgates for the Ørsted mission [31], as well as the Astrid-2 and MAGSAT missions [32].

In the case of the Ørsted mission and other magnetometers, the thin shell of magnetic fields was created by altering the total field experienced by the magnetometer using a set of test coils such as the Technical University of Braunschweig Magnetsrode coil system, with a specified accuracy of 1 nT for field components when the field was the same strength as the geomagnetic field [31]. In other cases, a set of accurate test coils was not available and the thin shell of magnetic measurements was created by rotating the magnetometer within the background geomagnetic field. This technique was used for the calibration of a tensor magnetic gradiometer by [30] and for the simultaneous calibration of a triaxial fluxgate magnetometer and an accelerometer by [33], as well as for the calibration of AUV magnetometers by [34].

Thin shell calibration is a suitable calibration technique for surface vessel magnetic signature measurements. The deviation in the background magnetic field due to the surface vessel magnets as recorded at AUV locations is small, generally under 2000 nT, relative to the background field of $\sim 55,000$ nT. Thus the magnetic field vectors recorded during measurement are very close to an area of the thin shell used for calibration.

In-Situ Calibration Data Acquisition

The first type of calibration is termed in-situ calibration, and is conducted at the deep-water testing facility in a clean magnetic environment: the AUV runs a submerged mission in which it circles about the same position several times, varying pitch, roll, and yaw through a range of angles larger than those expected during the mission. This in-situ calibration is somewhat analogous with the in-flight calibrations used on the Ørsted spacecraft, which obtained a fit of 0.33 nT RMS to the scalar reference field using a more complex model than the one described in this text with 27 coefficients incorporating temperature dependence and time-derivatives of the other parameters [31]. An overhead view of a typical in-situ AUV magnetometer calibration run is shown in Fig. 11. Since the AUV did not send any navigation pings in order to preserve a clean magnetic field, no reference positions or onboard EKF positions were available for this run. Positions were determined by an early iteration of the post-processing EKF using the onboard compass and propeller RPM measurements.

Since the AUV is weighted for stability and the fins have limited control authority, the roll and pitch angles experienced by the AUV do not cover all possible values. The magnetic field vectors recorded only cover a small portion of the thin shell, as shown in Fig. 12 for a typical in-situ calibration run. The rationale for in-situ calibrations is that collecting calibration data at the same aqueous environment, physical location, and approximate time as the actual magnetic signature mission mitigates

many potential error sources, such as temperature effects and variations in the magnetometer system over time, that could not be otherwise considered in a relatively simple calibration. Since the magnetometer was only exposed to a small section of the thin shell of field vectors, the calibration was not expected to be accurate over the entire thin shell.

Land Calibration Data Acquisition

When it became apparent that the in-situ calibrations were not effective, the author began searching for a way to expose the magnetometer to a complete shell of magnetic field orientations in a clean magnetic environment. This was not possible in-situ because the AUVs have limited control authority as well as built-in safety systems which abort any maneuver with pitch or roll angles significantly

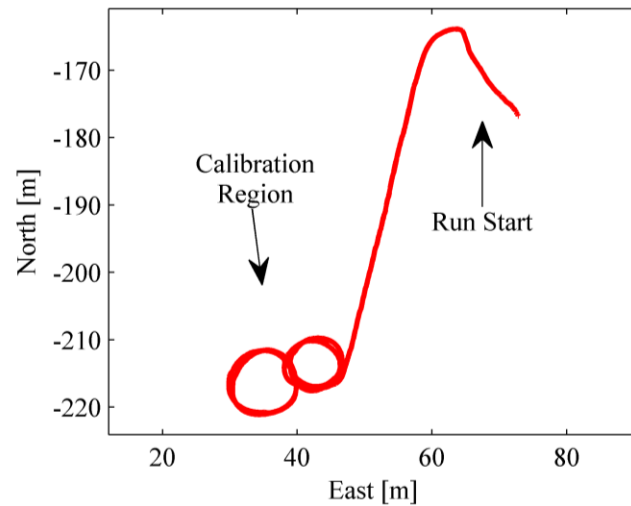


Figure 12. Overhead view of AUV positions during in-situ calibration. The AUV navigates away from any magnetic disturbances near the run start such as the surface vessel before beginning the calibration.

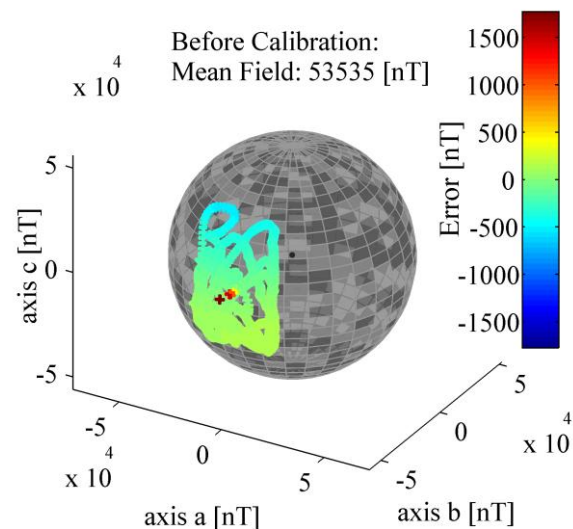


Figure 11. Partial thin shell of measured magnetic field vectors in magnetometer reference frame before and after calibration procedure. Data acquired during in-situ calibration.

different than those experienced during normal operation. An additional problem with in-situ calibrations was that magnetic noise from the motor also degraded the quality of the calibration signal.

Due to a limited timeframe and budget, it was not possible to build a complex nonmagnetic calibration system, but it was possible to build a manually operated calibration apparatus. First a location was found at the University of Idaho campus where the background magnetic field was spatially constant and where an overhanging non-magnetic support was available. This location was found by examining magnetic field gradients at various locations around the campus using a cesium total field gradient magnetometer until an area was discovered with both a low magnetic field gradient and an overhead support for a calibration apparatus. In the particular location chosen for land calibrations, the support was provided by a sturdy tree branch and the magnetic gradient magnitude was measured to be less than 15 nT per meter. The precise location of the testing site on the Administration building lawn was [48.9032° North, -119.1290° East].

During these land calibrations, a nonmagnetic calibration system shown in Fig. 13 was attached to the overhead supporting tree branch and used to position the AUV through a set of rotations. The rotations included a discrete set of five to six calibration apparatus pitches and a complete, continuous range of yaw and roll values such that the AUV magnetometer was exposed to the ambient geomagnetic field in almost all solid angle regions. Energy to rotate the AUV was provided by manually twisting a long nonmagnetic shaft attached to the center ring of the apparatus shown in Fig. 13.

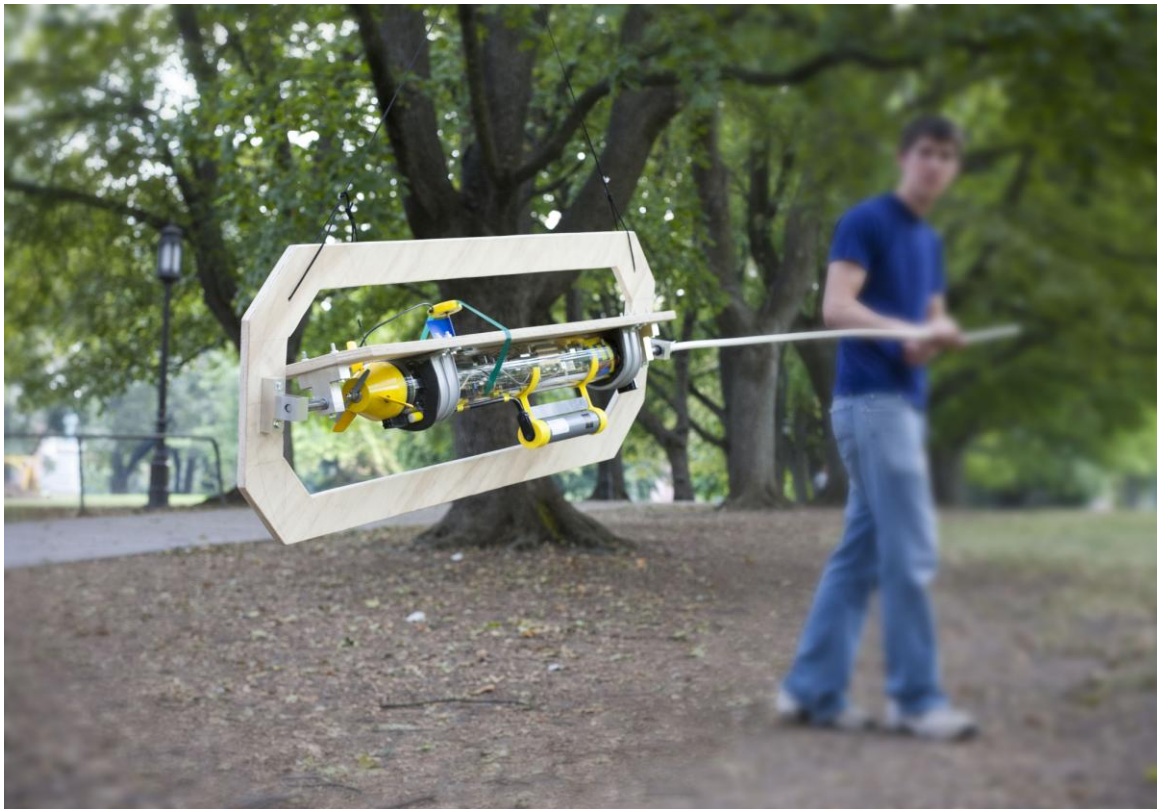


Figure 13. Non-magnetic calibration apparatus holding AUV during land calibration operated by an undergraduate research assistant.

Calibration Coefficient Optimization Algorithm

A simplex optimization algorithm implemented in MATLAB was applied to in-situ or land calibration data to find the optimal calibration coefficients. The calibration coefficients $\alpha, \beta, \gamma, a_d, a_e, a_f, b_d, b_e, b_f$ were varied by the optimization function until the mean squared error e for the n measurements in a calibration $e = \frac{\sum_n |\vec{B}_m| - |\vec{B}_r| |^2}{n}$ between the measured field magnitudes $|\vec{B}_m(\alpha, \beta, \gamma, a_d, a_e, a_f, b_d, b_e, b_f)|$ and a reference field magnitude $|\vec{B}_r|$ was minimized. Ideally the reference field magnitude $|\vec{B}_r|$ would have been measured repeatedly during the calibration procedure by a very accurate scalar magnetometer to account for any variations in the background geomagnetic field. Although a cesium total field magnetometer was available to provide verification of the total field measurement, it was only intermittently functional in practice and could not be used to reliably provide a time-dependent reference field $|\vec{B}_r|$ during magnetic calibrations. Thus the reference magnetic field during the calibration run was assumed to remain constant, a fairly safe

assumption considering the time scale used in a calibration of approximately 5-10 minutes. The magnitude of the reference field was based on the magnitude of the field measured by the magnetometer without the benefit of the calibration model. This uncalibrated field \vec{B}_u was determined by applying the ideal magnetometer model to the magnetometer voltages acquired during the calibration procedure, $\vec{B}_u = \vec{B}_m(\frac{\pi}{2}, \frac{\pi}{2}, \frac{\pi}{2}, 80000, 80000, 80000, 0, 0, 0)$. The reference field magnitude $|\vec{B}_r|$ was simply found from the mean value of the resulting n uncalibrated field measurements $|\vec{B}_r| = \frac{\sum_n |\vec{B}_u|}{n}$. This method constrained the mean magnitude of the field after calibration to equal the mean magnitude of the uncalibrated field.

Additionally, scale errors introduced into a particular magnetometer system by relying on this technique were easily normalized in post-processing in cases where multiple AUV magnetic measurements were combined. Single AUV measurements were used as-is, but further processing was required to combine magnetic measurements by multiple AUVs because the mean fields measured by the AUVs differed by up to several thousand nT. When multiple AUVs were used simultaneously for magnetic measurements, each vector field measurement was multiplied by a constant scalar correction factor for each AUV such that the mean magnitude of the magnetic measurements for a specific AUV matched the expected background field magnitude according to the World Magnetic Model predictions at the deep water testing range and the approximate date of testing [26].

The optimal calibration coefficients were found using the simplex algorithm *fminsearch()* function in MATLAB. The algorithm required an initial guess for the calibration coefficients, which was a random sample drawn from a normal probability distribution *randn* with a mean:

- Non-orthogonality angles: $\frac{\pi}{2} + 0.1 * randn$; *radians*
- Linear scale factors for each axis: $80000 + 100 * randn$; $\frac{nT}{volt}$
- Constant offsets for each axis: $100 * randn$; *nT*

The randomized initial conditions were used to ensure that the solution for $\alpha, \beta, \gamma, a_d, a_e, a_f, b_d, b_e, b_f$ converged for several different optimizations. As discussed in Chapter 6, the convergence of the solution in the *fminsearch()* algorithm depended strongly on whether the data was collected during a land calibration or an in-situ calibration.

Chapter 6: Magnetic Results

Signal De-spiking and Filtering Results

The techniques described in Chapter 5 successfully eliminated most of the magnetic excursions due to navigation pings and high frequency noise. The magnetic deviation measurements in Fig. 14 for a characteristic moving surface vessel pass by a single AUV include raw, filtered, and filtered and calibrated magnetic data and demonstrate that the filtering and calibration procedures greatly improve the quality of the data. The magnetic signature of the surface vessel source is only clearly visible after both filtering and calibration. The raw data is shown in red and generally contains about 200 nT of noise, with 17 additional brief downward excursions due to navigation pings. The filtered magnetic data in blue successfully eliminated the navigation pings and reduces high frequency noise while preserving the low frequency signal in the raw data. Finally the magnetometer calibration removes the orientation-dependent measurement errors displayed in the filtered magnetic data seen throughout the AUV pass. While the excursions in calibrated data at the center of the run correspond to the surface vessel pass, the measurements away from the surface vessel were expected to contain a constant field magnitude: the fluctuations in the calibrated magnetic data away from the surface vessel are due to the imperfect magnetometer model and remnants of the navigation ping disturbances.

The beginning of the run in Fig. 14 displayed a much larger amount of noise in raw, filtered, and calibrated field deviation measurements, as was the case for almost every AUV run. During this section of the run the AUV motor was turned on and the AUV dove underwater. The exact cause of this noise was unknown, although it could have been caused by fluctuating power supply voltages or noise due to motor or servo operation. The magnetometer could have been particularly susceptible to noise due to its single-ended rather than differential signaling. This noise was not deemed to be significant because it never occurred at the same time as magnetic measurements.

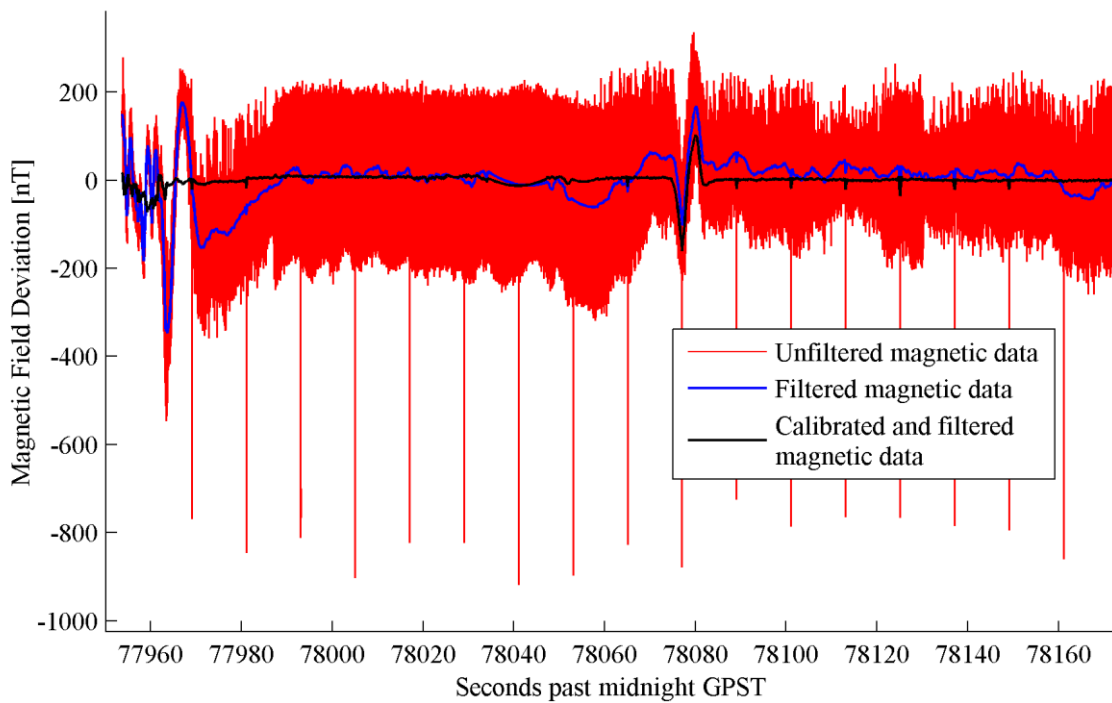


Figure 14. Comparison of raw magnetic data, filtered magnetic data, and calibrated magnetic data.

In-Situ Calibration Results

Although the in-situ calibration only used data from a small portion of the entire thin shell as in Fig. 12, it was expected that since the in-situ calibration would expose the AUV to a significantly wider range of magnetic field angles than the actual magnetic signature measurement, the in-situ calibration would still produce excellent results for the magnetic fields measured during a surface vessel measurement. Testing showed that this was not the case: without a large portion of the thin shell available during calibration, the calibration coefficient error surface did not appear to have a global minimum with a well defined error curve surrounding it: separate calibrations using identical data and slightly different optimization initialization conditions converged to very different solutions. Table 2 demonstrates that the calibration coefficient optimization function produced widely different results for calibration coefficients from separate optimization on a single in-situ calibration mission using slightly different initial coefficient guesses. Even in the range of angles expected to be seen by the AUV magnetometer during a magnetic signature measurement, the in-situ calibration performed poorly.

Table 2. In-Situ Magnetometer Calibration Coefficients

Coeff	Unit	AUV 2			Ideal
		Calibration 1	Calibration 2	Calibration 3	
α	(rad.)	1.573	1.573	1.573	1.5708
β	(rad.)	1.564	1.564	1.564	1.5708
γ	(rad.)	1.569	1.569	1.569	1.5708
a_x	nT/V	79,622	79,686	79,691	80000
a_y	nT/V	79,802	79,938	79,949	80000
a_z	nT/V	80,858	80,923	80,927	80000
b_x	nT	-344	-687	620	0
b_y	nT	-432	39	535	0
b_z	nT	-444	96	553	0
Mean error	nT	2.25	2.26	2.26	0

Note that calibration coefficients are not consistent between three calibrations based on identical data. The mean error is measured over the data acquired during the in-situ calibration.

Land Calibration Results

Land-based calibrations have been performed for each magnetometer-equipped AUV used for the testing described in this text, and these are the calibrations applied to magnetic data throughout the paper unless otherwise noted. Table 3 shows the magnetometer coefficients for each AUV derived from the land calibration procedure. A complete thin shell of magnetic data acquired during land calibrations always resulted in unique solutions for calibration coefficients using the calibration coefficient optimization function and magnetometer model described in Chapter 5. The calibration coefficient optimization attempts to minimize errors by varying the coefficients whether the errors are internal to the magnetometer or caused by the voltage divider, AUV, or other source. Thus each calibration is only applicable for a specific AUV/DSP/voltage divider/magnetometer combination. This also means that a difference between a particular calibration coefficient found by the optimization function and the ideal coefficient for a perfect system may be caused by more than a single component such as a fluxgate or voltage divider.

When the land calibrations were performed, it was expected that the Land calibrations would only be effective for measurement data from the same approximate time and temperature based on the temperature-dependent calibrations in [35], but it was found that a single Land calibration sufficed for AUV runs at varying water temperatures and testing dates separated by

months or years.

Table 3. Land Magnetometer Calibration Coefficients

<i>Coeff</i>	<i>Unit</i>	AUV 2	AUV 7	AUV 8	AUV 9	Ideal
α	(rad.)	1.57305	1.57176	1.57343	1.57011	1.5708
β	(rad.)	1.56331	1.57115	1.56880	1.57221	1.5708
γ	(rad.)	1.56878	1.57780	1.57859	1.57499	1.5708
a_x	nT/V	80,756.5	79,988.5	79596.4	83,924.4	80000
a_y	nT/V	79,624.2	79,585.6	80,698.3	80,074.3	80000
a_z	nT/V	79,929.1	81,671.3	79,585.3	77,246.5	80000
b_x	nT	-257.928	33.234	127.713	-158.169	0
b_y	nT	-50.968	87.527	-77.540	-127.268	0
b_z	nT	206.392	91.297	55.159	-10.286	0
RMS Uncalibrated Error	nT	276.5	200.2	269.2	1064.7	0
RMS Calibrated Error	nT	5.21	3.34	10.02	14.91	0

Note that the RMS errors for AUVs 2 and 7 did not include data taken during manual adjustments of the calibration apparatus.

The calibration coefficients representing magnetometer axis angles, α, β, γ , are all close to the desired 90° within 0.5° . This result matches the manufacturer's specification of orthogonality error of less than 1° . The gain coefficients for each axis i , a_i , are all within 1.5% of the nominal value except for the gain coefficients a_x and a_z for AUV 9 which were both approximately 5% from the nominal value of $80,000 \frac{nT}{V}$. The constant offset coefficients for each axis i , b_i , are all within several hundred nT of the ideal value, 0 nT. Because a single Land calibration sufficed for a wide variety of testing conditions, time and temperature did not appear to affect the magnetometer significantly.

The following figure, Fig. 15, contains magnetic data taken during a Land calibration routine at varying orientations before and after calibration. The uncalibrated field data contains five sections of data with different mean field magnitudes corresponding to the five discrete pitch settings of the calibration apparatus, varying from ~ -75 degrees to $\sim +75$ degrees relative to the horizon. Each of the five sections of data acquired at unique calibration apparatus pitches is indicated in the figure. Within each of these sections of data, approximately two large fluctuations in uncalibrated field magnitude are visible, corresponding to two consecutive and continuous rotations of the calibration apparatus about the yaw axis. The direction of yaw motion was reversed after one complete rotation. Finally, the most rapid fluctuations in field magnitude were caused by continuous rotation of the calibration apparatus around its roll axis. Fig. 15 demonstrates that the

MATLAB calibration function was able to find calibration coefficients which reduced the orientation-dependent sensor error by more than two orders of magnitude. The reference field used for calibration was the mean filtered field, which prevented the calibration procedure from altering the mean amplitude of the measured field.

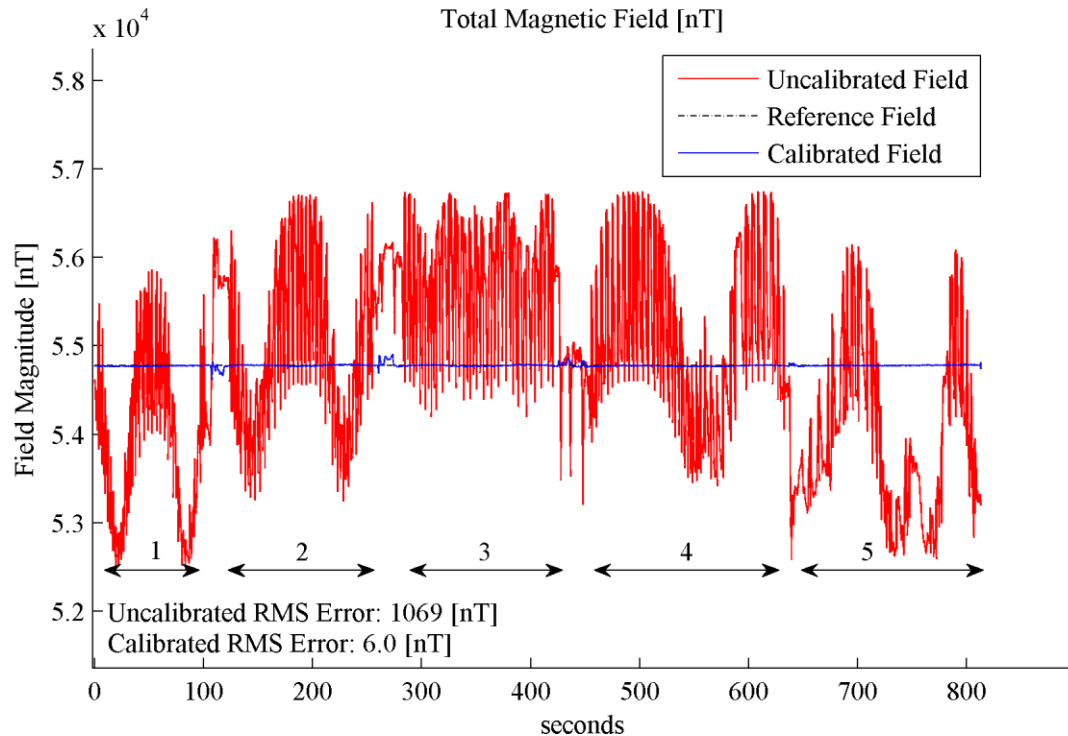


Figure 15. Pre- and post-calibration filtered magnetic signal acquired during land calibration.

The set of magnetometer orientations used during the calibration did an excellent job of capturing a thin shell of magnetic measurements. Figure 16 illustrates the thin shell of filtered magnetic fields before and after calibration as a set of points where each point corresponds to a particular magnetic field measurement. The location of each point in the magnetometer reference frame was determined by the field components of the magnetic field along each fluxgate axis such that an external measurement of AUV orientation was not necessary. The fluxgate axes also provide the axes for the figure. The gaps at the poles of the thin shells are due to the limited range of pitch angles available to the calibration apparatus. The thin shell poles are also not aligned with any of the magnetometer axes because the geomagnetic field vector is not aligned with the gravity vector. A clear orientation-dependent error of thousands of nanotesla is visible in the uncalibrated thin shell. The calibrated thin shell demonstrates that this large-scale orientation dependent error has been

removed and that the remaining errors have a much more complex structure. In actual magnetic source measurement runs, the range of field orientations in the magnetometer's reference frame is much smaller than the complete shell in this calibration, so the uncalibrated measurements have less apparent error than the calibration data: Fig. 14 demonstrates that the improvement in field measurement gained by calibration is not generally as dramatic as the improvement in Fig. 15.

The simple magnetometer model used in this text would not have been able to remove the residual errors in the calibrated field thin shell. Previous work by [31] has been done mapping errors on this thin shell to a more complex calibration using a spherical harmonic model for the fluxgate axes. The author carried out a preliminary study of this approach, but the improvement in performance was too small to warrant further study at the time.

Additionally, some of the errors in the calibrated thin shell are due to manual adjustments of calibration apparatus pitch during the calibration procedure. While the operator was generally several meters away from the AUV and had no known magnetic sources on his person, adjusting the calibration apparatus to each new discrete pitch setting required the operator to walk up to the apparatus. Since the time duration of these adjustment events was small compared to the total calibration time, no post-processing was used to trim these adjustment events from the calibration data. These events may be seen in Fig. 15 as brief spikes for the calibrated field between the data sections illustrated 1-5 in the figure. They may also be seen in Fig. 16 as tracks of data with a large error in orientations other than the general orientations of the other data paths. Since the errors in this data were due to a completely unknown source, the magnetometer model could not account for them.

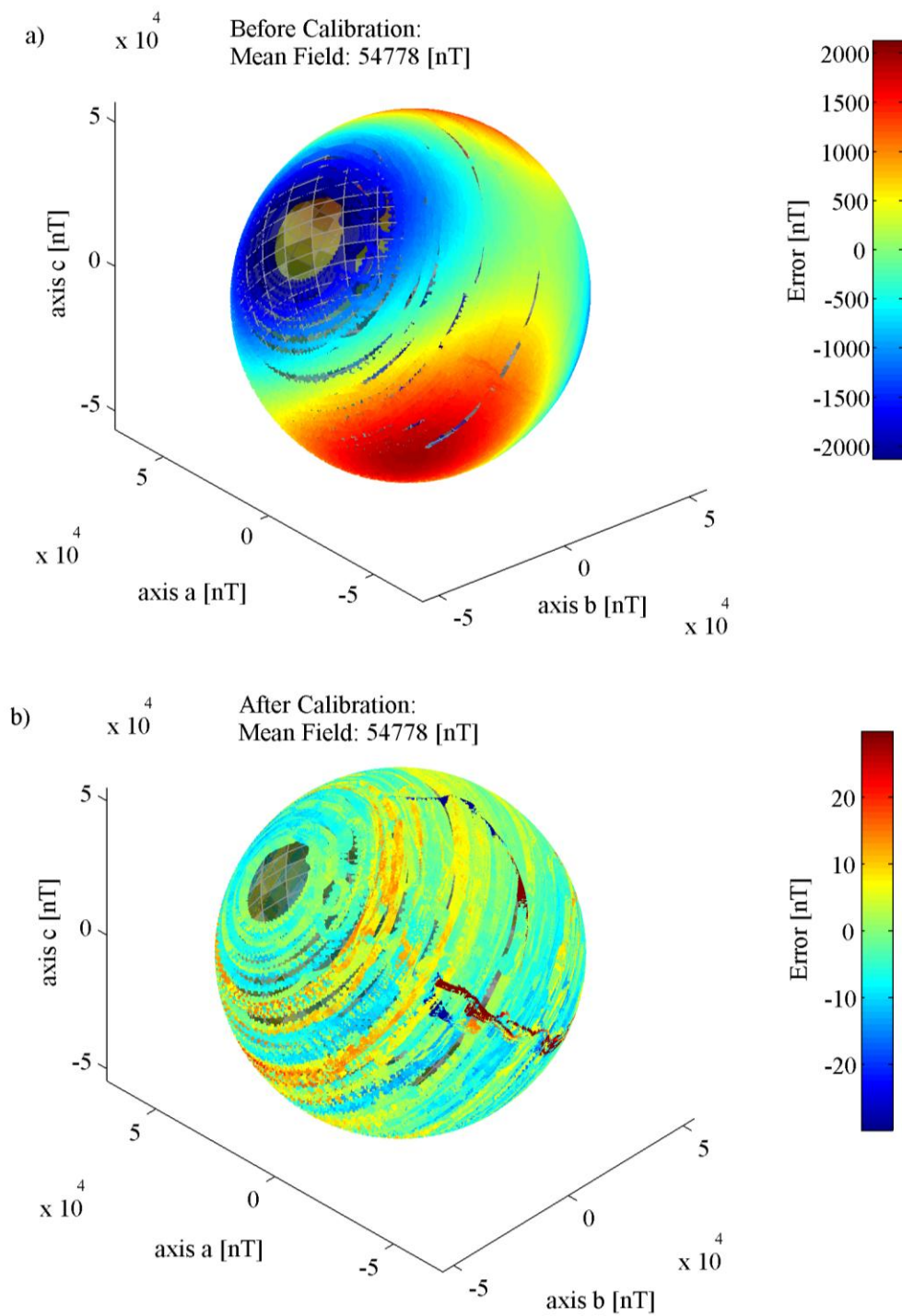


Figure 16. Thin shell of measured magnetic field vectors in magnetometer reference frame before and after calibration procedure. Data acquired during land calibration.

Chapter 7: Magnetic Signature Mapping Results

Several sets of magnet signature measurements of the fixed source and moving surface vessel were completed on Feb 24, 2012. The data from these runs was used to create overhead views of AUV magnetic measurement paths in Fig. 18 and Fig. 21 as well as approximate interpolated field maps for the fixed source and moving surface vessel in Fig. 17 and Fig. 20. A single AUV broadcast intermittent leader messages to other AUVs in the fleet for all magnet passes, resulting in intermittently corrupted data for that AUV.

The overhead measurement paths were created by interpolating 10 Hz magnetic measurements and 4 Hz AUV position measurements to a common set of timestamps spaced at 7 Hz and plotting a box for each resulting point. The measurement path locations were transformed into the relative frame of the magnetic source under consideration. Greyscale representations of the surface vessel and buoy are shown at the appropriate positions. The buoy magnet was mounted in the center of the buoy and the surface vessel magnet was mounted on the front of the surface vessel. Leader broadcasts were not removed from the magnetic signature measurements because they may be easily observed as the intermittent pulses.

The field map surfaces were created by interpolating all magnetic and position measurements to a common set of timestamps at 4 Hz and creating a Delaunay triangulation of the resulting vertices. A surface was created from the triangulation with color determined by linearly interpolating the field deviation magnitudes at surface vertices. Since each field map was composed of two sequential fleet passes, two AUV paths have intermittent invalid magnetic data for each field surface, one from each fleet pass. This invalid magnetic data was removed after the creation of the approximate field surface, as can be seen in Fig. 17 where two AUV tracks have intermittent gaps.

Fixed Magnetic Source Map

The buoy field map in Fig. 17 is displayed in the global reference frame with horizontal positions relative to the buoy and vertical positions relative to the water surface. The AUVs navigated at depths of ~3-4 meters, while the buoy magnet, not shown, was fixed at a depth of ~9.1 meters. The data is taken from two sequential buoy fleet passes. In each fleet pass the AUVs passed the magnet while navigating on a westerly heading and then reversed course and passed the

magnet while on an easterly heading. All AUV position data was provided by the independent reference position system.

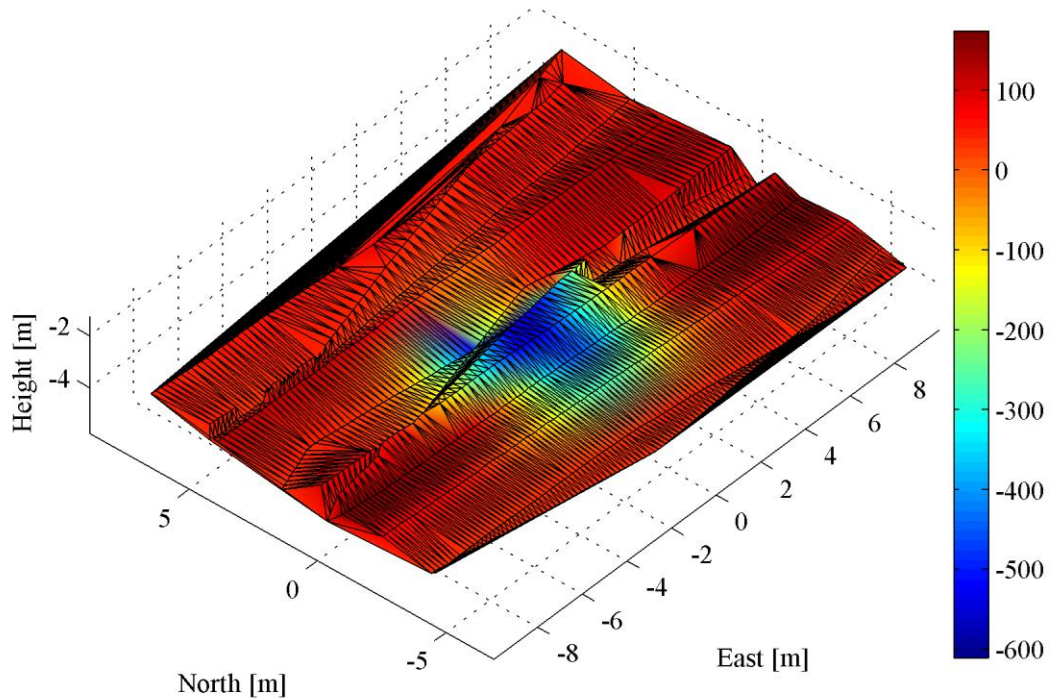


Figure 17. Perspective view of interpolated buoy field map surface using topside positions.

The paths traced by each AUV during the magnetic measurement may be seen in more detail in Fig. 18, an overhead view of interpolated AUV positions and magnetic measurements without any additional interpolation surface. Leader broadcasts were not removed from Fig. 18 and are visible as blue pulses in the magnetic field magnitude. Since the reference positions were only available intermittently, linear interpolation between reference positions caused the AUV paths to have a jagged appearance. The second image was created using post-processing positions: the AUV paths are much smoother because the post-processed data was available at a high frequency, but the post-processing EKF positions in this figure have a mean error of 1.96 meters with respect to the reference positions. The paths near the buoy do not line up well with the expected shape of the magnetic deviation when compared to the paths produced by interpolated reference positions.

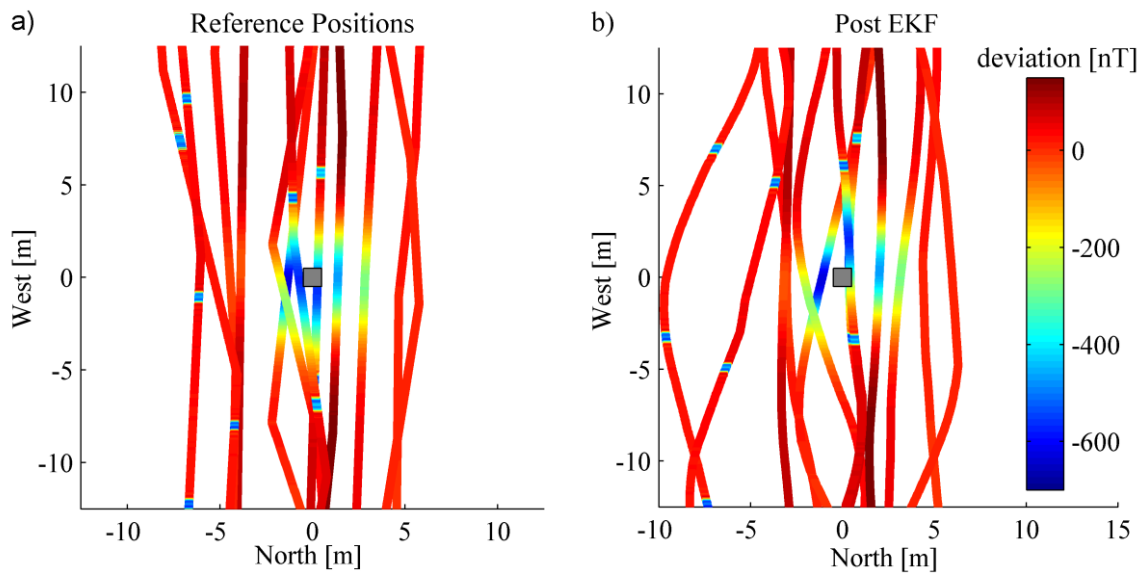


Figure 18. Overhead view of buoy field measurement paths according to topside and post-processing EKF positions.

Surface Vessel Field Map

Magnetic measurements of the surface vessel were taken by AUVs during two fleet passes. Although the fields measured near the bow of the AUV matched the predicted fields, the field deviations measured near the stern of the surface vessel were larger than predicted by the field model. This error was believed to be caused by the inherent magnetic field of the surface vessel concentrated near the stern. Although the surface vessel had a fiberglass hull, a magnetic signature was expected due to the motors and other equipment.

A single surface vessel pass was taken during initial measurements without the known magnetic source mounted to the front of the surface vessel as shown in Fig. 19. Just as with the fixed buoy passes, leader broadcast pings were removed from the surface field map in Fig. 20 but not the field measurement path in Fig. 21. While much of the variation in the illustrated magnetic signal is due to residual noise from navigation pings and an imperfect calibration, the large excursion of about ~ 80 nT magnitude is due to the inherent magnetic field of the surface vessel measured by the AUV as it navigated underneath the surface vessel at a depth of 2.5 meters. A similar peak can be found in all other plots of surface vessel field disturbance vs. time, although the total field disturbance in all other figures is the result of a vector addition of this inherent field, the known dipole field, and the background geomagnetic field.

The surface vessel field map in Fig. 20 is displayed in a reference frame relative to the surface vessel, where horizontal positions are relative to the surface vessel magnet and vertical positions are relative to the surface of the water. The approximate shape of the surface vessel is shown in grey on the water surface, with red lines indicating the approximate location of the dipole. The actual location of the dipole was generally about ~ 0.3 meters above the water surface, depending on surface vessel configuration. The data in this surface vessel field map was derived from two consecutive surface vessel pass missions in each of which three AUVs navigated under the surface vessel as a fleet, in a formation described in more detail in Chapter 2. While the field excursion under the surface vessel bow has approximately circular contours as expected from the dipole model illustrated in Fig. 8, the excursion due to the inherent magnetic field of the surface vessel can clearly be seen under the stern, where the measured deviation of up to ~ 150 nT cannot be accounted for by the known dipole field.

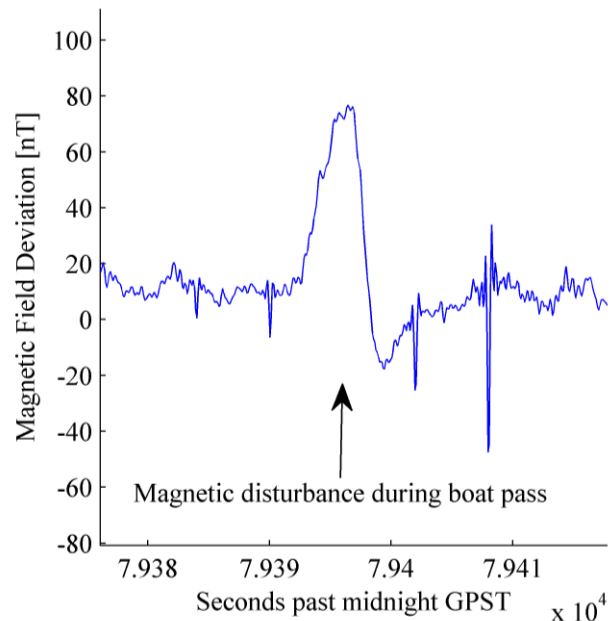


Figure 19. Magnetic field measurement during surface vessel pass without additional known magnetic source.

Although the desired AUV paths were spaced evenly underneath the surface vessel, the field map has few AUV paths directly underneath or on the starboard side of the surface vessel and many AUV paths underneath the port side of the surface vessel. There are two sources of these relative positioning errors. Because the AUVs navigated relative to a predefined waypoint path rather than the true position of the surface vessel, navigation errors on the surface vessel affected the relative positions of the AUVs. Additionally, only the onboard EKF was available to the AUVs during navigation and they used an imperfect control algorithm, so their true paths did not match their desired paths.

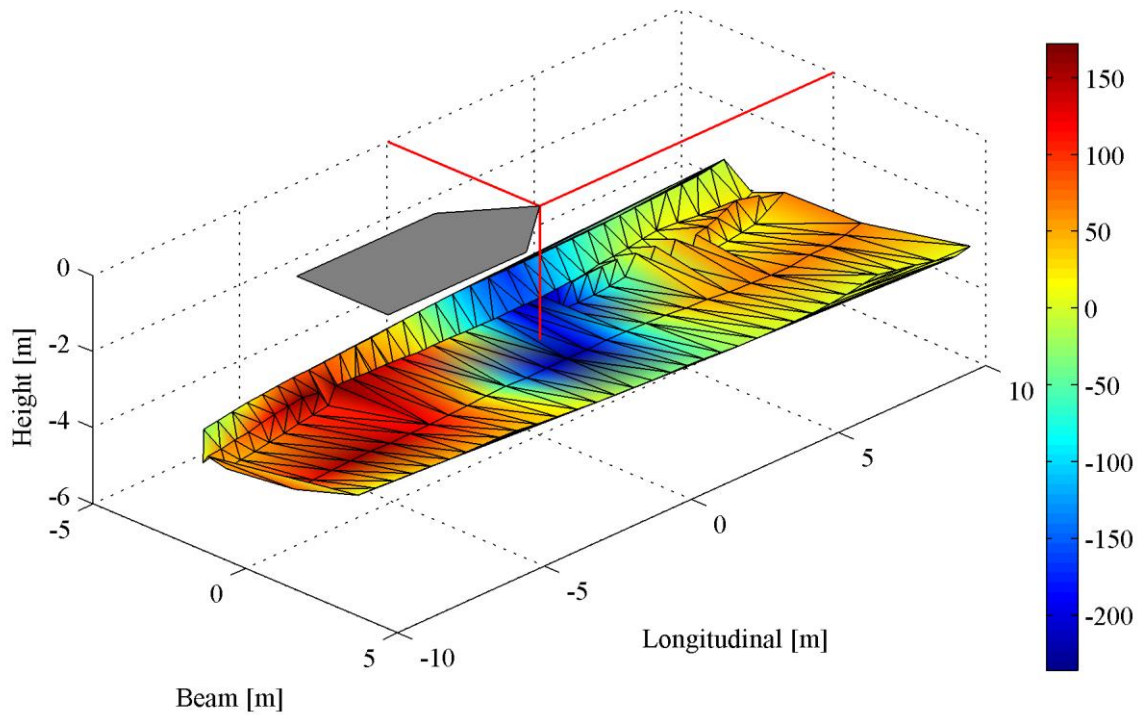


Figure 20. Perspective view of interpolated surface vessel field map surface using post-processing EKF positions

An overhead view of the AUV paths is provided in Fig. 21 which shows the variation between AUV positions estimated by the post-processing EKF and the reference position system. Observation of the AUV path with a visible leader broadcast disturbance in the magnetic field shows that position estimates differ significantly for this specific run, well above the mean post-processing EKF error for general AUV missions of 1.38 meters. The beam or lateral difference in the location of the navigation ping was 3.1 meters, while the longitudinal difference was 1.5 meters, combining to create a total horizontal position error of 3.4 meters. The rest of the post-processing position estimates of AUV paths in this field map were much closer to the typical post-processing EKF performance with a mean error relative to reference positions of 1.44 meters.

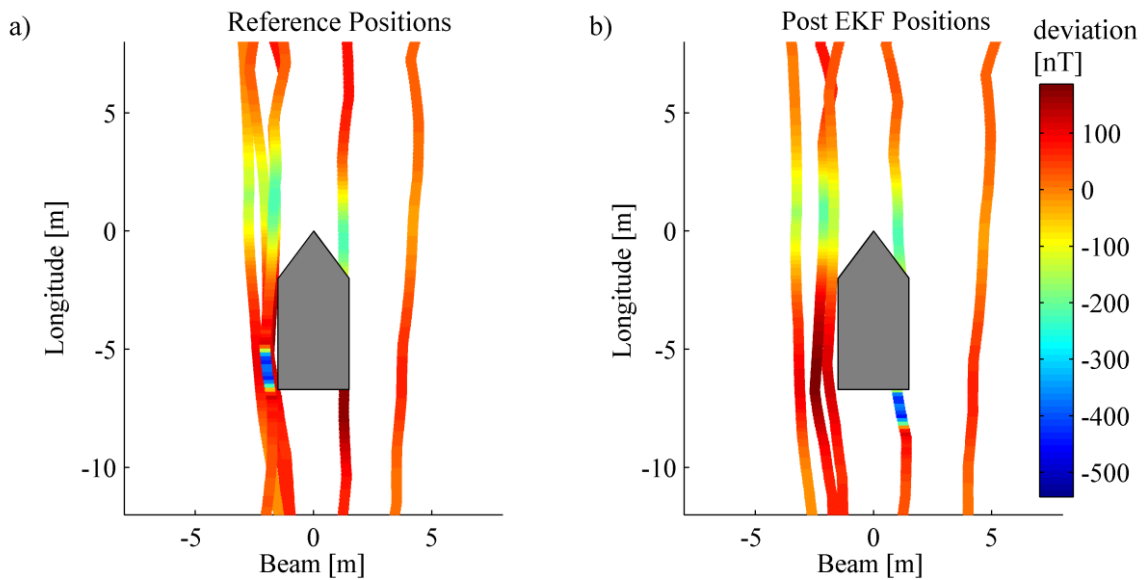


Figure 21. Overhead view of surface vessel field measurement paths according to topside and post-processing EKF positions.

Error Propagation Theory

Both position errors and magnetometer measurement errors have an effect on the final error between the true field at a point relative to the surface vessel and the measured field believed to correspond to that point. An error propagation function was created in order to determine the total error during magnetic measurement passes when the magnetic measurements were acquired by calibrated magnetometers and the AUV positions were found using the post-processing smoothed position estimates. The error propagation used here is based on the discussion and notation in [36].

Consider a system with input normally distributed random variable x with mean μ_x and standard deviation σ_x and an output random variable y , where x and y may both be vectors. It is not a simple matter to find the effect of uncertainty in x on the uncertainty of $y = f(x)$ if $f(x)$ is a nonlinear function, although the following approximation may be used.

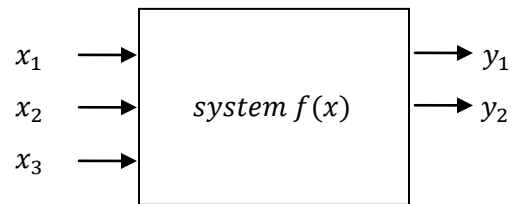
Let $f(x)$ be approximated as a Taylor series about the point $x \approx \mu_x$ as

$$y \approx f(\mu_x) + \left. \frac{\partial f}{\partial x} \right|_{x=\mu_x} (x - \mu_x).$$

The mean and standard deviation of $f(x)$ may be approximated as the following functions of the mean and standard deviation of x ,

$$\mu_y = f(\mu_x), \sigma_y = \left. \frac{\partial f}{\partial x} \right|_{x=\mu_x} (\sigma_x).$$

This approach may be generalized for a system with multiple input random variables and output random variables, as illustrated below.



In this case, a Taylor series approximation of $f(x)$ may be created by using the Jacobian:

$$J = \text{jacobian}(f, x) = \frac{\partial(f_1, f_2, \dots, f_n)}{\partial(x_1, x_2, \dots, x_m)}$$

If the independent variables have the covariance matrix,

$$C_x = \begin{bmatrix} \sigma_{x_1}^2 & \dots & \dots \\ \dots & \sigma_{x_2}^2 & \dots \\ \dots & \dots & \dots \end{bmatrix},$$

Then the dependent variables have the covariance matrix,

$$C_f = \begin{bmatrix} \sigma_{f_1}^2 & \dots & \dots \\ \dots & \sigma_{f_2}^2 & \dots \\ \dots & \dots & \dots \end{bmatrix} = J * C_x * J^T.$$

In order to apply this Taylor approximation of uncertainty propagation on the AUV acquired magnetic data, the following assumptions are used:

- The background geomagnetic field is a perfectly known uniform static vector.
- The dipole locations and orientations are known perfectly.
- The surface vessel navigates in exact cardinal directions.
- The dipole magnitudes and orientations are known perfectly.
- The magnetometer measurement uncertainty is treated as an additive Gaussian noise v_m applied to the true magnetic field. This is a reasonable assumption based on the approximately

constant magnetic field magnitude during magnetic signature measurement missions. This assumption allows the use of calibration performance statistics for error propagation.

Given these assumptions, the scalar uncertainty in a field measured by an AUV in the vicinity of a surface vessel may be modeled as:

$$y = |\vec{B}_{measured}| = |\vec{B}_g + \vec{B}_m(\vec{m}, \vec{x}_m, \vec{x}_A)| + v_m.$$

The background geomagnetic field is based on a prediction from the World Magnetic Model 2010 for the latitude, longitude, and elevation of the Bayview testing area:

$$B_g = [4,854 \quad 17,571 \quad 52,287]^T \text{ nT}.$$

The predicted source field was calculated using the dipole model described in Chapter 5 and experimental data for the dipole source magnitude \vec{m} and location \vec{x}_m . The dipole was assumed to be oriented vertically. While interpolated post-processing AUV positions were used to find the expected field due to the experimental data, the AUV positions \vec{x}_A used in the error propagation were determined by the independent reference AUV positions. The rationale for this choice was that the error propagation was intended to evaluate operational measurement performance, in which case no reference positions would be available and the post-processing AUV position estimates would be the best position estimates to determine the expected field due to the dipole. The error propagation, on the other hand, depends strongly on the actual gradient of the magnetic field at actual AUV positions rather than the expected gradient at estimated AUV positions, so independent reference positions were used to provide more accurate positions for the error propagations.

$$\vec{m} = [0 \quad 0 \quad m_z]^T \quad [Am^2]$$

$$\vec{x}_m = [E_m \quad N_m \quad Z_m]^T \quad [meters].$$

$$\vec{x}_A = [E_A \quad N_A \quad Z_A]^T \quad [meters].$$

Since all other variables were considered perfectly known quantities, the random variables considered for error propagation were

$$x = [\vec{x}_{AUV} \quad v_m]^T = [E_A \quad N_A \quad Z_A \quad v_m]^T.$$

As the error propagation was intended to evaluate operational performance, the standard deviation for each of these variables was based on conservative estimates of post-processing position accuracy, depth measurement accuracy, and magnetometer accuracy based on the RMS errors experienced during magnetometer calibrations

$$\sigma = [2 \text{ meters} \quad 2 \text{ meters} \quad 0.2 \text{ meters} \quad 5 \text{ nT}]^T$$

$$C_x = \begin{bmatrix} (2 \text{ meters})^2 & 0 & 0 & 0 \\ 0 & (2 \text{ meters})^2 & 0 & 0 \\ 0 & 0 & (0.2 \text{ meters})^2 & 0 \\ 0 & 0 & 0 & (5 \text{ nT})^2 \end{bmatrix}$$

For each point in the runs considered for uncertainty propagation, the mean value for AUV position measurements was provided by experimental data and the mean value for the magnetometer calibration noise was 0 based on the calibration approach described earlier:

$$\mu = [E_A \quad N_A \quad Z_A \quad 0]^T.$$

The Jacobian J was found as described above

$$J = \frac{\partial y}{\partial x} = \frac{\partial(|\vec{B}_g + \vec{B}_m(\vec{m}, \vec{x}_m, \vec{x}_A)| + v_m)}{\partial x}.$$

It was too lengthy to display in analytical terms. Analysis performed using this method demonstrated that the expected error in AUV measurements depended greatly on the proximity of the AUV to the source. Characteristic error propagations are shown for a surface vessel pass and two fixed buoy passes. Since the AUV was closer to the source during the surface vessel pass, the navigation uncertainty was more significant for these measurements.

Error Propagation Results: Surface Vessel Pass

During the AUV surface vessel pass magnetic signature missions, the AUVs passed under the magnetic source at a depth varying from approximately three to four meters. The error propagation for a single surface vessel pass by a single AUV is shown in Fig 22. The predicted magnetic field deviation in this figure was based on post-processing EKF AUV position estimates, and the error between the measured and predicted field deviation is based on this same post-processing estimate of AUV positions. The error budget curve of the error standard deviation was based on reference AUV positions.

Since the error propagation and the dipole model do not include the effects of the unknown surface vessel magnetic source, there is a large difference between predicted and measured fields after the main field around 78077 seconds in Fig. 22 due to the unknown source. Within the area dominated by the known dipole, however, the error propagation curve provides an upper bound for the field measurement error.

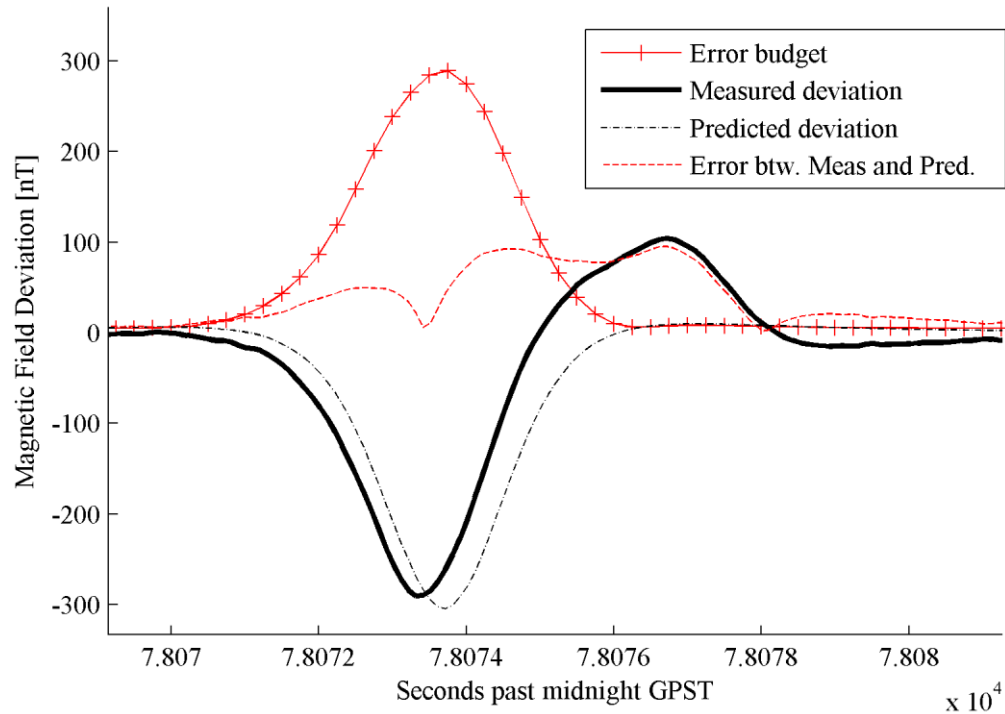


Figure 22. Error propagation of surface vessel pass by single AUV. AUV and surface vessel navigated in opposing directions.

Error Propagation Results: Buoy Pass

In the case of the buoy passes, the AUVs passed above the magnetic source at a relative height of approximately six meters. The increased distance of the AUVs from the magnetic source is partially responsible for the smaller effect of position uncertainty on total uncertainty compared to surface vessel passes. An additional effect is due to the differing source strengths: as described in Chapter 4, the source used for the buoy pass was 448 Am^2 , while the source used for the surface vessel pass was only 135 Am^2 . Thus the AUV positioning accuracy required for an accurate surface vessel pass was higher than the accuracy required for a buoy pass. Fig. 23 shows that the AUV field

matches the predicted field very well: unlike the surface vessel, the buoy had no known inherent magnetic fields. Additionally, the error between measured and predicted field closely was similar to the expected error due to the error propagation. As with the surface vessel error propagations, predicted field magnitudes used the post-processing EKF estimates of AUV position while the error propagation used the AUV reference position measurements.

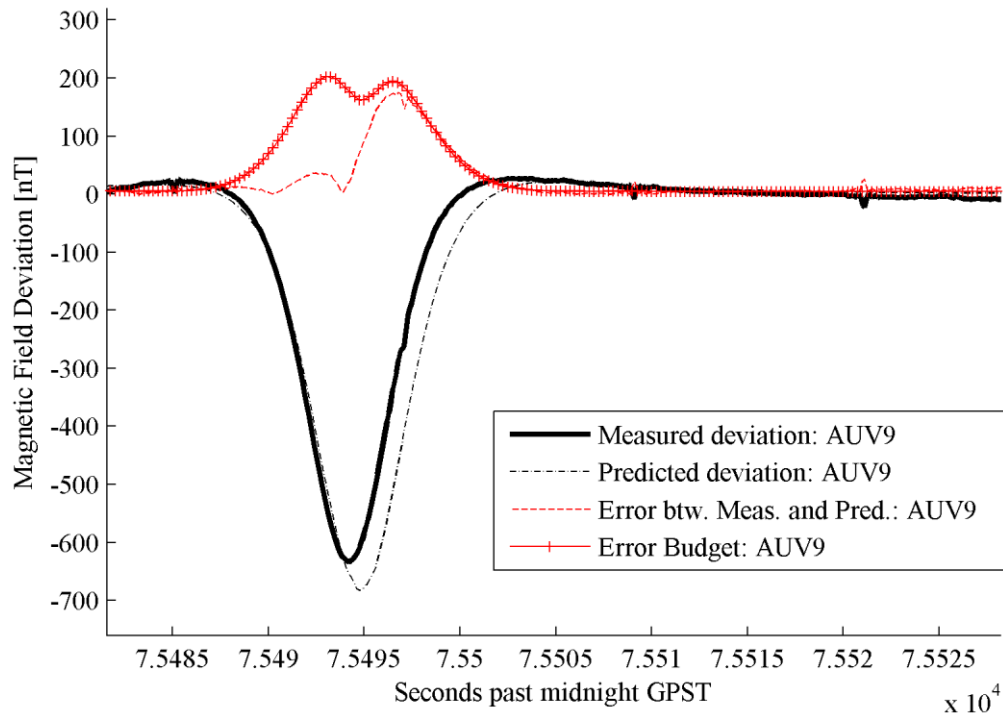


Figure 23. Error propagation of buoy pass by single AUV.

Another characteristic error propagation of a fixed buoy pass by a single AUV is shown in Fig. 24. In this case the actual error between measured and predicted field was significantly smaller than the error propagation predicted, an indication that the navigation was better than expected. Due to the error propagation model, magnetometer errors increase the error budget by a constant amount for any particular magnetic measurement, while the error budget due to post-processing position error depends strongly on the location of the AUV relative to the magnet.

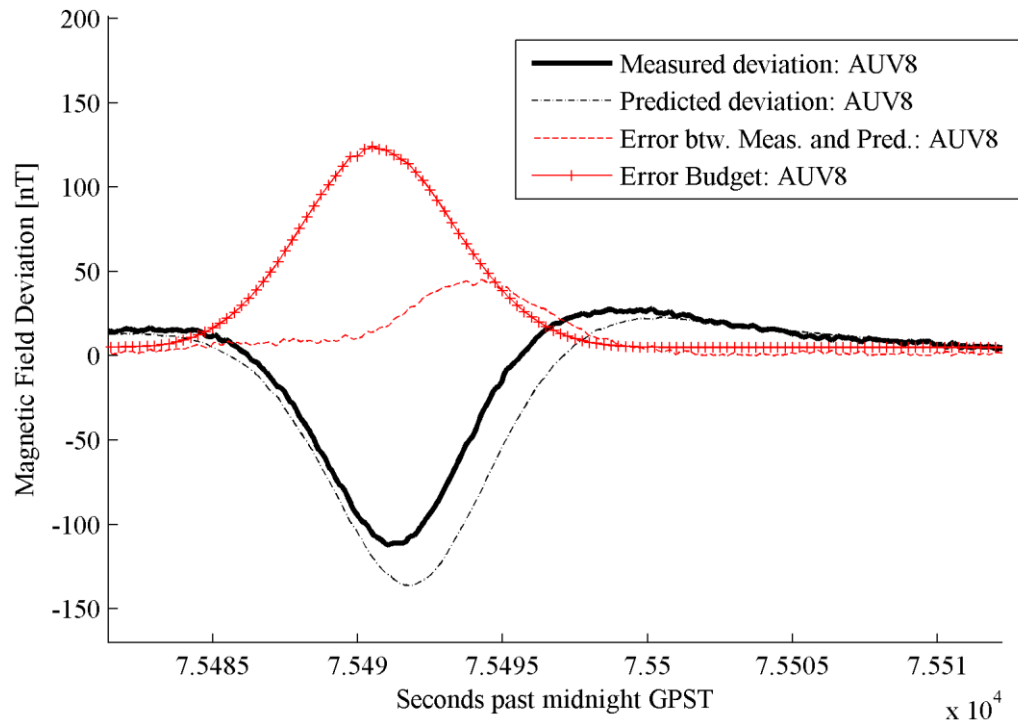


Figure 24. Error propagation of buoy pass by single AUV.

General Error Propagations

If the constraint that the ship's field is created by a single dipole is relaxed and the calculations are generalized to an arbitrarily large number of unknown dipoles, the ability to analytically calculate the error function or a Taylor series approximation is lost. Some of the information required to create an error propagation, such as the field gradients, can be approximated along a single direction using data from an AUV surface vessel pass, but this is insufficient information. If an additional AUV passes along the same horizontal plane as the first AUV, the gradient along approximately horizontal orthogonal axes may be estimated, but the vertical component of the gradient cannot be estimated given this information, even if it were known that the source was a single dipole. For example, both the direction of AUV motion and a perpendicular direction to a nearby measurement by another AUV at a given AUV measurement point could lie along a field magnitude isosurface, such as those shown in Figs. 7 and 8 showing the shape of field disturbance isosurfaces caused by magnetic dipoles. In this case, the field gradient measured along these two axes could be negligibly small, but the field gradient along a

perpendicular axis could still be arbitrarily large. One potential method to circumvent this problem would be to make the assumptions that the field gradient will be similar in all directions, and that AUV depth uncertainty is far smaller than AUV horizontal positioning uncertainty. In this case, the effects of vertical field gradient and AUV depth uncertainty may be neglected in the error propagation.

If it is also known that there is a minimum distance between the magnetometers and the magnetic sources along a given axis during magnetic measurements, as is the case during any reasonable surface vessel characterization mission, additional assumptions may be made about the field gradients experienced by the AUV. Error propagations based on these assumptions would be interesting material for future work.

Error Budget and Significance of Accuracy for Measurements

Both the AUV position estimation system and the AUV magnetometer measurement system have inherent inaccuracies. These inaccuracies have been reduced by calibrating and post-processing the data, but some inaccuracies remain. It is of interest for future potential research and system optimization to determine whether one particular error source is the limiting factor on total system inaccuracy. If this is the case, more effort should be spent optimizing the performance of that particular source of error.

According to the assumptions about measurement errors and the model used in the error propagation, AUV position uncertainty is responsible for much more measurement error than magnetic measurement uncertainty. This is due to the large magnetic gradients in the vicinity of the magnetic source: small errors in AUV position estimates have large effects on the predicted field. The relative importance of position estimation accuracy and magnetometer accuracy depends strongly on the magnetic source characteristics, and further work to improve the magnetic signature measurement system described in this document will depend on the magnetic signature measurement mission under consideration

Chapter 8: Conclusions

Project Status

The AUV Magnetic Signature Measurement Project has successfully demonstrated that a fleet of AUVs in the deep water testing range can measure the magnetic signature of a surface vessel with position accuracy close to the desired 1 meter position error and magnetometer accuracy much better than the desired accuracy of 25-100 nT. This performance was achieved primarily by calibrating the magnetometer, allowing a magnetic field measurement accuracy of 5-10 nanotesla, and by post-processing AUV data using an extended Kalman filter and acausal RTS smoother in order to reach a horizontal position accuracy of 1.3 meters.

Fleets of magnetometer-equipped AUVs have measured the magnetic signatures of a fixed magnetic buoy and a moving surface vessel. In both cases the measured magnetic fields closely matched the magnetic fields predicted by a dipole model of the magnetic sources, although an additional field was measured under the stern of the surface vessel that was not predicted by the dipole model for the magnetic source on the bow of the surface vessel.

Future Research

The dipole-based error propagations worked well for the research in this document, but it would be useful to create an error propagation that used AUV-measured magnetic field gradients and relaxed the constraint of dipole sources. It would also be useful to improve the quality of the AUV post-processing position estimation methods so that the position estimation accuracy met or exceeded the 1 meter goal. Finally, it would also be useful to demonstrate a navigation method that did not require an accurately surveyed set of underwater buoys such as those used in the deep water range. Preliminary work on navigation relative to buoys mounted to the surface vessel has been completed in [11], but further advances will be necessary to meet the navigation accuracy goals for the project.

While the work by the University of Idaho AUV team has demonstrated the general feasibility of an AUV fleet magnetic measurement system, the AUV system used for research is not appropriate for operational use. In order to create a more robust system, several changes should take place in the AUV system architecture, hardware, and software. Several University of Idaho researchers are currently working on migrating the AUV system to a more advanced hardware and

software platform. With these modifications, the AUVs will be suitable for operational measurements of naval surface vessels and will fulfill the end goal of assisting the Navy in the protection of surface vessels.

References

- [1] John J. Holmes, *Exploitation of Ship's Magnetic Field Signatures*. San Francisco: Morgan & Claypool Publishers, 2006.
- [2] John J. Holmes, *Modeling a Ship's Ferromagnetic Signatures*. San Francisco: Morgan & Claypool Publishers, 2007.
- [3] Daniel Stilwell, Aditya Gadre, Caleb Sylvester, and Christopher Cannel, "Design elements of a small low-cost autonomous underwater vehicle for field experiments in multi-vehicle coordination," *IEEE/OES Autonomous Underwater Vehicles*, pp. 1-6, 2004.
- [4] Jesse Pentzer et al., "Measurement of Magnetic Field Using Collaborative AUVs," in *IEEE/Oceans*, Sydney, 2010.
- [5] Benjamin Armstrong et al., "Field Measurement of Surface Ship Magnetic Signature Using Multiple AUVs," in *IEEE Oceans*, Biloxi, 2009.
- [6] Christopher Walker et al., "Calibration and Localization of AUV-acquired Magnetic Survey Data," in *IEEE Oceans*, Kona, 2011, pp. 1-6.
- [7] P. Baccou and B. Joenvencel, "Homing and navigation using one transponder for AUV, post-processing comparisons results with Long Base-Line navigation," *Proc. IEEE Conf. on Robotics & Automation*, pp. 4004-4009, 2002.
- [8] S. McPhail and M. Pebody, "Range-Only Positioning of a Deep-Diving Autonomous Underwater Vehicle From a Surface Ship," *IEEE Journal of Oceanic Engineering*, pp. 669-677, 2009.
- [9] A. Bahr, J. Leonard, and M. Fallon, "Cooperative Localization for Autonomous Underwater Vehicles," *The International Journal of Robotics Research*, pp. 714-728, 2009.
- [10] N. Kussat, C. Chadwell, and R. Zimmerman, "Absolute Positioning of an Autonomous Underwater Vehicle using GPS and Acoustic Measurements," *IEEE Journal of Oceanic Engineering*, pp. 153-164, 2005.

- [11] Amanda Folk et al., "Autonomous Underwater Vehicle Navigation using Moving Baseline on a Target Ship," in *Proceedings of MTS/IEEE*, Seattle, 2010.
- [12] Jordan Q. Stringfield, "Autonomous Underwater Vehicles: Navigation Utilizing Short Baseline Techniques," Moscow, 2012.
- [13] R. Eustice, H. Singh, and L. Whitcomb, "Synchronous-Clock, One-Way-Travel-Time Acoustic Navigation for Underwater Vehicles," *Journal of Field Robotics*, pp. 121-136, 2011.
- [14] Brendan Crosbie, Michael Anderson, Eric Wolbrecht, John Canning, and Dean Edwards, "Synchronous Navigation of AUVs Using WHOI Micro-Modem 13-bit Communications," in *Proceedings of Oceans '10*, Seattle, 2010.
- [15] J. Curcio et al., "Experiments in Moving Baseline Navigation using Autonomous Surface Craft," in *Proc. IEEE/MTS Oceans Conf. Exhib.*, Washington, D.C., 2005.
- [16] R. Eustice, L. Whitcomb, H. Singh, and M. Grund, "Experimental Results in Synchronous-Clock One-Way-Travel-Time Acoustic Navigation for Autonomous Underwater Vehicles," in *IEEE International Conference on Robotics and Automation*, Rome, 2007, pp. 4257-4264.
- [17] M. Fallon, G. Papadopoulos, and J. Leonard, "Cooperative AUV Navigation using a Single Surface Craft," *Field and Service Robotics*, 2009.
- [18] Jesse Pentzer et al., "Spatial Sampling of Magnetic Field Using Collaborating Autonomous Underwater Vehicles," *Battlespace Acoustic and Magnetic Sensors*, 2010.
- [19] Doug Odell, Jesse Pentzer, John Canning, and Dean Edwards, "A Versatile Tracking System for AUV Testing," in *IEEE Oceans*, Sydney, 2010.
- [20] Benjamin Armstrong, Eric Wolbrecht, and Dean Edwards, "AUV navigation in the presence of a magnetic disturbance with an extended Kalman filter," in *OCEANS*, Sydney, 2010, pp. 1-6.
- [21] Dan Simon, *Optimal State Estimation*. Hoboken: Wiley Interscience, 2006.

- [22] H. Rauch, F. Tung, and C. Striebel, "Maximum Likelihood Estimates of Linear Dynamic Systems," Reston, 1965.
- [23] O. Nielsen et al., "Development, construction and analysis of the 'Ørsted' fluxgate magnetometer," *Meas. Sci. Technol.* 6, pp. 1099-1115, 1995.
- [24] James Lenz, "A Review of Magnetic Sensors," *Proceedings of the IEEE*, 1990.
- [25] Billingsley Aerospace & Defense, "TFM100g4-UHW / TFM200G4-UHW Underwater Triaxial Fluxgate Magnetometer," Germantown, 2008.
- [26] NGA, NGDC, BGS. (2009, December) World Magnetic Model WMM2010.
- [27] David Griffiths, *Introduction to Electrodynamics*. Upper Saddle River: Prentice Hall, 1999.
- [28] J. Merayo, P. Brauer, F. Primdahl, J. Petersen, and O. Nielsen, "Scalar calibration of vector magnetometers," *Meas. Sci. Technol.* 11, pp. 120-132, 2000.
- [29] P. Brauer, J. Merayo, O. Nielsen, F. Primdahl, and J. Petersen, "Transverse field effect in fluxgate sensors," *Sensors and Actuators A*, pp. 70-74, 1997.
- [30] Robert Bracken, David Smith, and Philip Brown, "Calibrating a Tensor Magnetic Gradiometer Using Spin Data," Reston, Virginia, 2005.
- [31] Torben Risbo et al., "Ørsted pre-flight magnetometer calibration mission," *Measurement Science and Technology* 14, pp. 674-688, 2003.
- [32] J. Merayo et al., "The Orthogonalization of Magnetic Systems," Lyngby,.
- [33] Vojtech Petrucha and Petr Kaspar, "Calibration of a Triaxial Fluxgate Magnetometer and Accelerometer with an Automated Non-magnetic Calibration System," in *IEEE Sensors*, Christchurch, 2009, pp. 1510-1513.
- [34] George Allen, John Purpura, and David Overway, "Measurement of Magnetic Noise Characteristics on Select AUVS with some Potential Mitigation Techniques," Panama City,.

- [35] P. Brauer, J. Merayo, T. Risbo, and F. Primdahl, "Magnetic Calibration of Vector Magnetometers: Linearity, Thermal Effects, and Stability," Lyngby,.
- [36] Kai Oliver Arras, "An Introduction To Error Propagation: Derivation, Meaning and Examples of $C_y = F_x C_x F_x^T$," Swiss Federal Institute of Technology Lausanne Departement de Microtechnique, Lausanne, 1998.

Appendices

Appendix 1: Log Structure Contents

For the sake of future contributors to the Magnetic Signature Measurement project, it may be useful to have a description of the standard AUV Log format and the purposes of its components. Each of the enumerated entries below is a field in the Log structure with a data source as described, and each of the bulleted subentries is a vector of numeric values or strings. In general, all of these values or strings are measured or created simultaneously as part of a packet, allowing a single timestamp vector within a field to store the timing of every packet. This list is based on previous work describing Log contents by Ben Wilson during his work at the University of Idaho as an undergraduate research assistant.

Log

1. sensr: data from AUV onboard text log regarding sensor measurements.

- t: Time of each sensor measurement [sec. past midnight GPST].
- heading: Heading measurement from the onboard compass [deg. east of N].
- pitch: Pitch measurement from the onboard compass [deg. east of N].
- roll: Roll measurement from the onboard compass [deg. east of N].
- dip: Angle at which the magnetic field crosses the horizontal plane [degrees].
- depth: Depth measured from the pressure sensor in the nose cone [meters].
- volts: Battery voltage, not functional.
- current: Battery current, not functional.
- charge: Remaining charge of the batteries, not functional.
- water: 0 if water detected inside AUV, 1 otherwise.
- yaw: Measurement from gyro on Spock, not functional.

- temp: Temperature of AUV circuit board [deg. C].
- long_deg: GPS longitudinal degrees converted to integer form [deg * 100000].
- lat_deg: GPS latitudinal degrees converted to integer form [deg * 100000].
- hour: Hour each sensr packet was received, found in Log parsing using the KirkLog timestamps [hours].
- min: Minute each sensr packet was received, found in Log parsing using the KirkLog timestamps [minutes].
- sec: Second each sensr packet was received, found in Log parsing using the KirkLog timestamps [seconds].
- gps_vel: Velocity according to the GPS sensor $\left[\frac{\text{meters}}{\text{second}}\right]$.
- gps_hpe: GPS horizontal position error [meters].
- gps_heading: Heading according to the GPS sensor [deg. east of N].
- x_accel: Acceleration of the sub in its local X direction from compass sensor $\left[\frac{\text{m}}{\text{s}^2}\right]$.
- y_accel: Acceleration of the sub in its local y direction from the compass sensor $\left[\frac{\text{m}}{\text{s}^2}\right]$.
- gps_pps_ms: GPS pulse per second measurement [ms].
- gps_north: North position from GPS data [meters].
- gps_east: East position from GPS data [meters].

2. cntrl: data from AUV onboard text log regarding AUV controls.

- t: Time of each cntrl packet [sec. past midnight GPST].
- motor_speed: commanded propeller speed [rpm].
- rudder: Angle of rudder fin [deci-degrees].
- elevator: Angle of elevator fin [deci-degrees].

- aileron: Angle of aileron fin [deci-degrees].
- wp_num: Current waypoint number.
- mode: AUV mode (dive, squat, GPS, etc.) as listed on printed mission list.
- path_north: North component of vector from waypoint n to waypoint n+1 [meters].
- path_east: East component of vector from waypoint n to waypoint n+1 [meters].
- est_north: North component of vector from zero point to AUV position [meters].
- est_east: East component of vector from zero point to AUV position [meters].
- targ_north: North component of vector from AUV position to the next waypoint [meters].
- targ_east: East component of vector from AUV position to the next waypoint [meters].
- href: The desired heading for the AUV to reach the next waypoint [deg. east of N].
- head_err: Difference between the actual AUV heading and href [deg. east of N].
- dist_path: Perpendicular distance from AUV position to path from last waypoint to next waypoint [meters].
- targ_length: Length of vector from zero position to AUV position [meters].
- total_prog: Total distance of travel to the next waypoint [meters].
- dist_rem: Distance left in the path from the previous waypoint to the next waypoint [meters].
- depth_int: Portion of integrator on depth controller.
- dist_int: Portion of integrator on distance controller.
- vel_est: Estimate of velocity based on motor RPM.

3. postn: data from AUV onboard text log regarding initial AUV positioning.

- t: Time of each postn packet [sec. past midnight GPST].
- north: Assumed initial north position of sub converted from GPS data [meters].
- east: Assumed initial east position of sub converted from GPS data [meters].
- time: Time after midnight in the form “HHMMSS”.
- buoymap: Sum of binary numbers describing which buoys provided ranges: a=1, b=2, c=4, d=8.
- range_a: Distance from sub to buoy a [meters].
- range_b: Distance from sub to buoy b [meters].
- range_c: Distance from sub to buoy c [meters].
- range_d: Distance from sub to buoy d [meters].

4. whmsg: data from AUV onboard text log regarding AUV acoustic communications.

- t: Time each Woods Hole Micro-modem (WHM) message is received and logged [sec. past midnight GPST].
- type: Type of message. 0 for 13 bit message, 1 for 32 byte message.
- src: Source of WHM message. 14, 15 for ship transponders, sub# for AUV.
- dest: Destination of WHM message, receiving AUV software ID.
- text: WHM message contents.
- north: North position of ship from encoded 13 bit WH message [meters].
- east: East position of ship from encoded 13 bit WH message [meters].
- speed: Speed of ship from encoded 13 bit WH message $\left[\frac{\text{meters}}{\text{second}}\right]$.
- heading: Heading of ship in 13 bit WH message [deg. east of N].

5. buoyp : data from AUV onboard text log regarding buoy locations and lake conditions.

- t: Time of each buoyp packet [sec. past midnight GPST].
- ssh2o: Speed of sound in water for that test [$\frac{\text{meters}}{\text{second}}$].
- zero_lat: Latitude of the origin of the local coordinate system.
- zero_long: Longitude of the origin of the local coordinate system.
- a_north: North position of buoy A relative to the origin [meters].
- a_east: East position of buoy A relative to the origin [meters].
- a_depth: Depth of buoy A [meters].
- b_north: North position of buoy B relative to the origin [meters].
- b_east: East position of buoy B relative to the origin [meters].
- b_depth: Depth of buoy B [meters].
- c_north: North position of buoy C relative to the origin [meters].
- c_east: East position of buoy C relative to the origin [meters].
- c_depth: Depth of buoy C [meters].
- d_north: North position of buoy D relative to the origin [meters].
- d_east: East position of buoy D relative to the origin [meters].
- d_depth: Depth of buoy D [meters].

6. speed: data from AUV onboard text log regarding motor driver performance.

- t: Time each speed packet was received [sec. past midnight GPST].
- rpm_percent: Percentage of commanded propeller RPM actually attained.

7. kalmn: data from AUV onboard text log regarding AUV localization filter performance.

- t: Time each kalman packet was received [sec. past midnight GPST].
- east: EKF estimate of AUV east position [meters].
- north: EKF estimate of AUV north position [meters].
- speed: EKF estimate of AUV speed [$\frac{\text{meters}}{\text{second}}$].
- heading: EKF estimate of AUV heading [deg. east of N].
- h_bias: EKF estimate of AUV heading bias [degrees].
- dt: Time between present EKF state estimate and previous state estimate [seconds]
- zgyro: Heading rate from the IMU rotated to the sub's local coordinates, [radians per second].
- Covariance matrix describing AUV state estimation confidence
 - cov_e: East covariance number for AUV EKF
 - cov_n: North covariance number AUV EKF
 - cov_u: Speed covariance number AUV EKF
 - cov_h: Heading covariance number AUV EKF
 - cov_b: Heading bias covariance number AUV EKF
 - cov_12: Covariance number for position (1,2) and (2,1)
 - cov_13: Covariance number for position (1,3) and (3,1)
 - cov_14: Covariance number for position (1,4) and (4,1)
 - cov_15: Covariance number for position (1,5) and (5,1)
 - cov_23: Covariance number for position (2,3) and (3,2)
 - cov_24: Covariance number for position (2,4) and (4,2)

- cov_25: Covariance number for position (2,5) and (5,2)
- cov_34: Covariance number for position (3,4) and (4,3)
- cov_35: Covariance number for position (3,5) and (5,3)
- cov_45: Covariance number for position (4,5) and (5,4)

8. kalms: data from AUV onboard text log regarding ship localization filter performance.

- t: Time of each kalms packet [sec. past midnight GPST].
- east: EKF estimate of ship east position [meters].
- north: EKF estimate of ship north position [meters].
- speed: EKF estimate of ship speed [$\frac{\text{meters}}{\text{second}}$].
- heading: EKF estimate of ship heading [deg. east of N].
- dt: Time between present EKF state estimate and previous state estimate [seconds].
- Covariance matrix describing ship state estimation confidence
 - cov_e: East covariance number for ship EKF
 - cov_n: North covariance number for ship EKF
 - cov_s: Speed covariance number for ship EKF
 - cov_h: Heading covariance number for ship EKF
 - cov_12: Covariance number for position (1,2) and (2,1)
 - cov_13: Covariance number for position (1,3) and (3,1)
 - cov_14: Covariance number for position (1,4) and (4,1)
 - cov_23: Covariance number for position (2,3) and (3,2)
 - cov_24: Covariance number for position (2,4) and (4,2)

- cov_34: Covariance number for position (3,4) and (4,3)

9. imu_t: data from AUV onboard text log regarding time-stamped IMU measurements.

- t: Time of each IMU measurement [sec. past midnight GPST].
- acc_x: Acceleration of sub in local X direction [$\frac{m}{s^2}$].
- acc_y: Acceleration of sub in local Y direction [$\frac{m}{s^2}$].
- acc_z: Acceleration of sub in local Z direction [$\frac{m}{s^2}$].
- rot_x: Angular rotation rate of sub about the local X axis [$\frac{radians}{second}$].
- rot_y: Angular rotation rate of sub about the local Y axis [$\frac{radians}{second}$].
- rot_z: Angular rotation rate of sub about the local Z axis [$\frac{radians}{second}$].

10. depth_t: data from AUV onboard text log regarding high-frequency pressure measurements (rare).

- t: Time of each depth_t packet [sec. past midnight GPST].
- depth_pressure: Depth of AUV [centimeters].

11. range: data from AUV onboard text log regarding acoustic transponder ranges

- t: Time each range measurement is received [sec. past midnight GPST].
- buoy: Number representing transmitting buoy. 1=a 2=b 3=c 4=d.
- cycle: not implemented.
- timestamp: Timestamp after midnight GPST rounded to nearest second provided by WHM as an integer representing "HHMMSS".
- arrival: time of arrival after top of second. Assumes transmissions are sent at top of second [seconds].

- distance: calculated distance from the sub to the transmitting buoy [meters].
- mode: Sum of mode integers, e.g. if second = 2, pulse = 1: mode = 3.
- quality: Received quality of message from WH modem [unknown units].
- Doppler: Doppler shift created by motion relative to buoy and water [unknown units].
- range_a: Range from buoy a for each transmission [meters].
- range_b: Range from buoy b for each transmission [meters].
- range_c: Range from buoy c for each transmission [meters].
- range_d: Range from buoy d for each transmission [meters].

12. ship: data from surface vessel differential GPS (dGPS) records supplied by Bayview.

- t: Time for each ship GPS measurement [sec. past midnight GPST].
- lat: Latitudinal degrees for the bow-mounted dGPS [deg].
- long: Longitudinal degrees for the bow-mounted dGPS [deg].
- speed: Speed of the ship according to the dGPS pair $\left[\frac{\text{meters}}{\text{second}}\right]$.
- heading: Heading of the ship according to the dGPS pair [deg. east of N].
- north: North position of bow-mounted dGPS
- east: East position of bow-mounted dGPS
- mode: Quality of the DGPS fix. 0: no fix, 1: GPS fix, 2: dGPS fix.

13. param: run metadata compiled from AUV log, additional sources.

- runStart: The start time for the run [sec. past midnight GPST].
- mission_no: The run mission number.

- run_no: The run number, a unique incrementing integer for a given AUV hardware ID and text log file.
- vehicle_pos: Vehicle position, 1=leader.
- software_id: The software AUV number.
- leader_flag: Boolean representing leader AUV: 0 = false, 1 = true.
- comms_mode: Communication mode for the run.
- hardware_id: AUV hardware identification number.
- date: Date of the run.
- transLoc: Transponder location, 'Yellow Barge' or 'In Bay'.
- lakeLevel: The height of the lake surface for the day, meters above sea level [meters].
- runEnd: The end time for the run [sec. past midnight GPST].
- Abort: The abort code for the run.

14. key: internal description of Log contents used to read and format AUV text logs.

- title: Title of Log field
- subpackets: expected number of subpackets
- cformat: expected format of packet information in the text log.
- Entry: Subfields for the title Log field.

15. ev: chronological list of Log events referencing other Log fields.

- t: Time for each event log entry [sec. past midnight GPST].
- n: field vector index for the specific event.
- p: name of field of specific event.

16. topside: data for reference positions supplied by Bayview.

- t: Time for each topside point [sec. past midnight GPST].
- raw: Raw data from Bayview-supplied topside parsing code.
- ping_time: Time at each topside ping, integer seconds [sec. past midnight GPST].
- sse1: Sum of squared errors, metric 1.
- sse2: Sum of squared errors, metric 2.
- ping_time_offset: Difference between the reception time and the ping time [seconds].
- north: topside-calculated north position of AUV at each topside point [meters].
- east: topside-calculated east position of AUV at each topside point [meters].
- depth: Depth of AUV at each topside [meters].

17. mag: AUV magnetometer measurements from binary AUV magnetometer logs.

- t: Time of each magnetic measurement [sec. past midnight GPST].
- Va: DSP voltage from a measurement signal along the magnetometer **a** axis [Volts].
- Vb: DSP voltage from a measurement signal along the magnetometer **b** axis [Volts].
- Vc: DSP voltage from a measurement signal along the magnetometer **c** axis [Volts].
- Bx: Calibrated magnetic field component in orthogonal x axis. [nT]
- By: Calibrated magnetic field component in orthogonal y axis. [nT]
- Bz: Calibrated magnetic field component in orthogonal z axis. [nT]
- a. B: Total calibrated measured magnetic field magnitude [nT].
- b. calCoeff: Calibration coefficients used for magnetic calibration.
- c. calFile: Filepath of magnetometer calibration file.

- d. pred: Sub-structure of predicted magnetic fields and gradients using dipole models and known sources.
- e. Bdev: Best estimate of the magnetic field with the mean subtracted [nT].

Appendix 2: Summary of MATLAB Code for Operations on AUV Data

All of the relevant MATLAB code is archived in a Subversion repository, currently located at: `svn+ssh://yourUserName@svn.mrc.uidaho.edu/projects/yelsub/SvnRepo2/MATLAB/` where “yourUserName” must be changed to a username with the appropriate SVN access permissions. Code for the entire AUV project can be found in other folders on this repository. The code generally acts on testing data stored on the yelsub server at `\\venus.mrc.uidaho.edu\Parsed AUV Data\`. This code falls into four broad categories, each stored in a separate folder within the SVN repository.

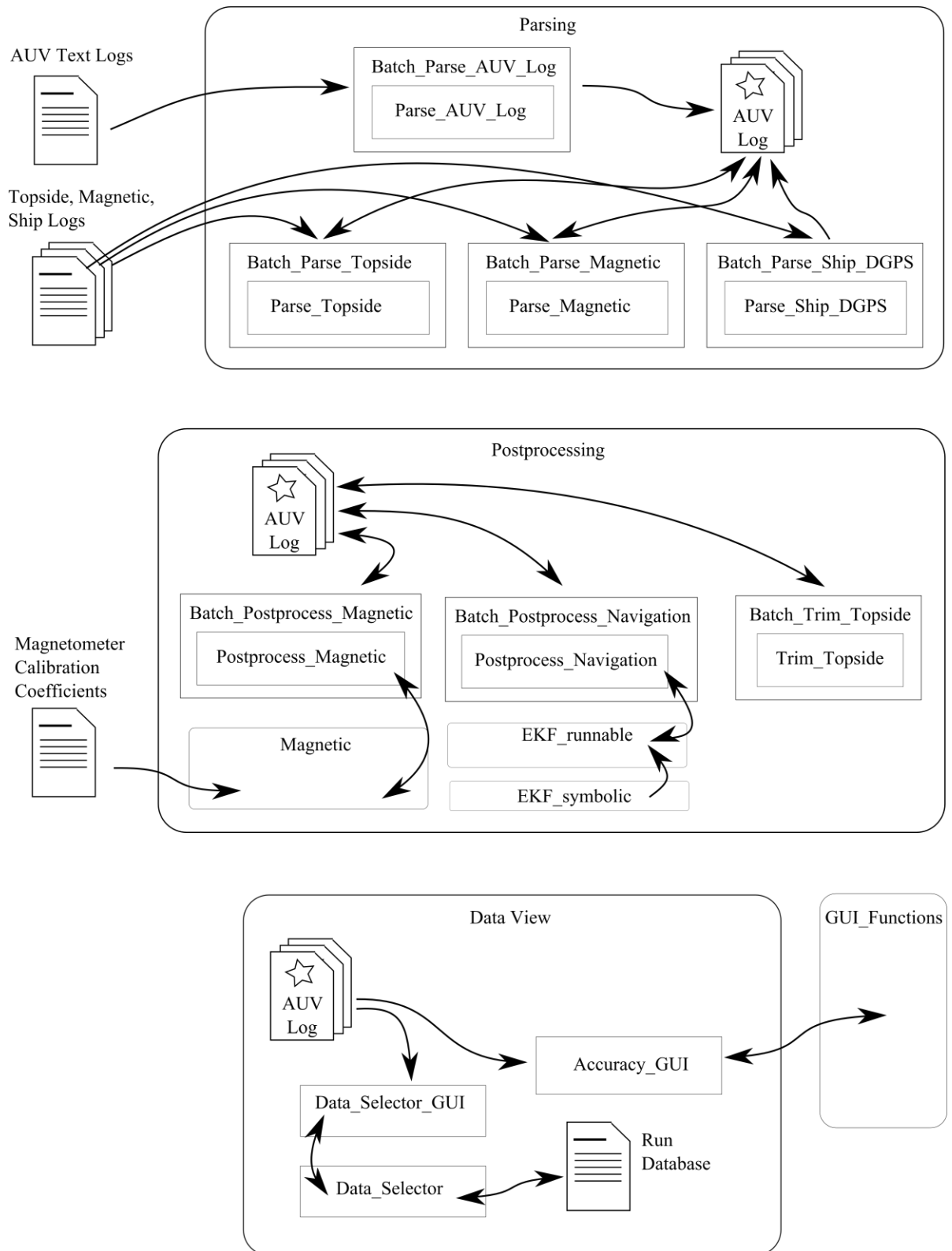
Parsing contains code generally intended to process text logs produced onboard AUVs during missions, binary logs containing binary magnetometer logs produced onboard AUVs during missions, topside tracking files produced by the reference tracking system at the deep-water or shallow-water testing ranges, and surface vessel dGPS data taken onboard the surface vessel and create a single MATLAB Log file, generally referred to as a Log file, for each AUV run with data from the above data sources. Parsing functions should integrate all relevant data into Log files and should clean up any errors present in the raw data, but they should not perform significant optional data post-processing functions: this restriction is intended to permit access to original Log data.

Postprocessing contains code generally intended to improve the accuracy of data already contained in a MATLAB Log file using various algorithms. For instance, there is code in the Postprocessing folder intended to improve position estimates for the AUV using a post-processing EKF and smoother, and additional code may be used to apply calibration models to the recorded magnetic data and find the measured magnetic fields. In general, post-processing functions may modify and save Log file data, but should not introduce new sources of experimental data.

Data View contains a set of graphical user interfaces and functions used to create a database referencing Log files, select Log files from the database according to desired criteria, browse through Log data, and/or display this data in the form of MATLAB figures. In general,

functions in Data View should not perform post-processing operations on source data from Log files and should not alter the original Log files.

GUI Functions is a supporting folder for Data View, containing backend functions that are referenced by the functions and GUIs in Data View.



Software Overview. The arrows indicate the direction of information flow.

Appendix 3: Extended Kalman Filter Theory

The equations described below are based on the notation in [21].

Nonlinear state update model as a function of previous state, previous control, and process noise

$$x_k = f_{k-1}(x_{k-1}, u_{k-1}, w_{k-1}).$$

Nonlinear measurement model as a function of current state and measurement noise

$$y_k = h_k(x_k, v_k).$$

Process noise is a zero-mean Gaussian with a known variance: $w_k \sim (0, Q_k)$.

Measurement noise is a zero-mean Gaussian with a known variance: $v_k \sim (0, R_k)$.

The filter state estimate is initialized with the expected state value

$$\hat{x}_0 = E\{x_0\}.$$

The a posteriori initial covariance of the state estimate error is the expected value of the error between actual initial state and initial a posteriori estimated state

$$P_{f0}^+ = E\{(x_0 - \hat{x}_0^+)(x_0 - \hat{x}_0^+)^T\}.$$

The EKF is subsequently iterated for $k = 1, \dots, N$ discrete time steps:

The previous state update model is linearized from the point of the previous a posteriori state estimate using a Jacobian

$$F_{k-1} = \left. \frac{\partial f_{k-1}}{\partial x} \right|_{\hat{x}_{k-1}^+}.$$

The previous state update noise-dependence is also linearized from the point of the previous a posteriori state estimate using a Jacobian

$$L_{k-1} = \left. \frac{\partial f_k}{\partial w} \right|_{\hat{x}_{k-1}^+}.$$

The current a priori state estimate is propagated from the previous a posteriori state estimate and control input with the assumption of zero noise

$$\hat{x}_k^- = f_{k-1}(x_{k-1}^+, u_{k-1}, 0).$$

The current a priori state estimate error covariance is updated based on the linearized state update model, the linearized state noise-dependence, the process noise variance, and the previous a posteriori state error estimate

$$P_k^- = F_{k-1}P_{k-1}^+F_{k-1}^T + L_{k-1}Q_{k-1}L_{k-1}^T.$$

The current measurement model is linearized from the point of the current a priori state estimate

$$H_k = \left. \frac{\partial h_k}{\partial x} \right|_{\hat{x}_k^-}.$$

The current noise dependence of the measurement model is linearized from the point of the current a priori state estimate

$$M_k = \left. \frac{\partial h_k}{\partial v} \right|_{\hat{x}_k^-}.$$

An intermediate K matrix is created

$$K_k = P_k^- H_k^T (H_k P_k^- H_k^T + M_k R_k M_k^T)^{-1}.$$

The current a posteriori state estimate is generated from a weighted combination of the current a priori state estimate and the intermediate K matrix multiplied by the residual between the measurement and the predicted measurements based on the a priori state estimate

$$\hat{x}_k^+ = \hat{x}_k^- + K_k [y_k - h_k(\hat{x}_k^-, 0)].$$

The a posteriori state error covariance is generated

$$P_k^+ = (I - K_k H_k) P_k^-.$$

Appendix 4: Rauch-Tung-Striebel Smoother Theory

Several variables are stored by the EKF during processing, allowing the RTS smoother to re-process the data in the reverse temporal direction. Using the notation in [21],

The final a posteriori state estimate is stored

$$\hat{x}_N = \hat{x}_{N_{EKF}}^+$$

The state estimate error covariance is also initialized from the final a posteriori value from the EKF

$$P_N = P_{N_{EKF}}^+$$

The RTS smoother then steps backwards through each of the time steps: *For* $k = N - 1, \dots, 0$

$$I_{k+1}^- = (P_{k+1}^-)^{-1}$$

$$K_k = P_k^+ F_k^T I_{k+1}^-$$

$$P_k = P_k^+ - K_k (P_{k+1}^- - P_{k+1}) K_k^T$$

$$\hat{x}_k = \hat{x}_k^+ + K_k (\hat{x}_{k+1} - \hat{x}_{k+1}^-).$$